This is the peer-reviewed, final accepted version for American Mineralogist, published by the Mineralogical Society of America.
The published version is subject to change. Cite as Authors (Year) Title. American Mineralogist, in press.
DOI: https://doi.org/10.2138/am-2022-8301. http://www.minsocam.org/

Word Count 9875

OXYGEN FUGACITY BUFFERING IN HIGH PRESSURE SOLID MEDIA ASSEMBLIES FROM IW-6.5 TO IW+4.5 AND APPLICATION TO THE V K-EDGE OXYBAROMETER.

Revision 2

Kevin Righter[1], Anna L. Butterworth[3], Zack Gainsforth[3], Christine E. Jilly-Rehak[3,4], Subhayan Roychoudhury[5], Kayla Iacovino[2], Richard Rowland[2], Timmons M. Erickson[2], Kellye Pando[2], Daniel K. Ross[2], David Prendergast[5], Andrew J. Westphal[3]

[1] Johnson Space Center, Houston, TX 77058; kevin.righter-1@nasa.gov.

[2] Jacobs-JETS, Johnson Space Center, Houston, TX 77058

[3] Space Sciences Laboratory, University of California Berkeley, Berkeley, CA 94720.

[4] Department of Geological Sciences, Stanford University, Stanford, CA 94305

[5] Molecular Foundry, Lawrence Berkeley National Laboratory, 1 Cyclotron Road, Berkeley CA 94720, USA

This is the peer-reviewed, final accepted version for American Mineralogist, published by the Mineralogical Society of America.
The published version is subject to change. Cite as Authors (Year) Title. American Mineralogist, in press.
DOI: https://doi.org/10.2138/am-2022-8301. http://www.minsocam.org/

Abstract - Control of oxygen fugacity during high temperature phase equilibrium experiments is required to simulate the conditions that exist in natural systems. At high pressures, oxygen fugacity may be imposed using solid buffer equilibria via the classic "double capsule" technique. This design becomes untenable, however, at temperatures above the melting points of commonly used noble metal capsule materials and/or where buffer assemblages may alloy with the capsule or contaminate the sample. Here we introduce and test a modified double capsule approach that includes a solid metal-oxide buffer in close proximity to but separate from the sample of interest. Buffers used include (in order of most oxidized to reduced) Ni-NiO, Co-CoO, W-WO_3, Fe-FeO, Mo-MoO_2, Cr-Cr_2O_3, V-V_2O_3, Ta-Ta_2O_5, and Nb-NbO. At a fixed temperature, these buffers span a wide range – up to 10 log fO_2 units. To demonstrate the buffering capacity of this double capsule approach, secondary redox equilibria and V-doped CaO-MgO-Al_2O_3-SiO_2 system glasses were studied in experiments using the double capsule geometry. The secondary equilibria provide an independent verification of the oxygen fugacity established in the double capsule environment. The glasses proved difficult to interpret, and our results provide guidance to future efforts to utilize the glass oxybarometer at reducing conditions. Application of this modified double capsule technique to studies of V valence in $MgAl_2O_4$ spinels led to the recognition of several factors that will affect V valence in this system: temperature of equilibration, duration of experiment, and spinel bulk composition. We have synthesized V-bearing $MgAl_2O_4$ spinel at the reduced conditions of the Cr-Cr_2O_3, (IW-3.51), Ta-Ta_2O_5, (IW-5.37), and Nb-NbO buffers (IW-5.44). This spinel exhibits a very small V^{3+} pre-edge peak consistent with its reduced nature. The absence of evidence for V^{2+} suggests that $MgAl_2O_4$ spinel excludes V^{2+} due to the preference of V for octahedral sites. This finding is supported by

45 DFT calculations for spinels of variable composition, and in agreement with some other indirect
46 evidence for preference for V^{3+} in aluminous spinels (Bosi et al. 2016; Paque et al., 2013).

Introduction

Oxygen fugacity (fO_2) is an intensive parameter that controls some fundamental chemical and physical properties in planetary materials (Righter et al., 2016). In terrestrial magmas, fO_2 is commonly in the range between the quartz-fayalite-magnetite (QFM) and Ni-NiO (NNO) buffers, where higher fO_2 promotes magnetite stability and lower fO_2 causes Fe-enrichment in liquids due to magnetite suppression during crystallization. In lunar and asteroidal basalts, fO_2 values are commonly much lower than those in terrestrial systems, i.e. significantly below the iron-wüstite (IW) buffer, and can stabilize metal. Meteorites that form the building blocks of planets range in mineralogic composition from the reduced, FeSi-metal-bearing enstatite chondrites to the oxidized magnetite-rich CK chondrites – spanning nearly 10 orders of magnitude in oxygen fugacity.

Understanding the redox state of cations that form under given fO_2 in relevant mineral assemblages provides a means of reading the recorded formation environment of ancient meteoritic materials. Previous experimental studies on cation valences in minerals and glasses have been carried out under relatively oxidized conditions relevant to terrestrial, martian, or lunar environments, but not at the reducing conditions relevant to solar nebular or other primitive chondritic materials. Application to such reduced materials has been limited by lack of low fO_2 standards.

Here, we report a new experimental approach that allows high temperature and pressure experimentation at reducing (as well as oxidizing) conditions. We then utilize this new approach to assess the usefulness of a Vanadium K-edge spectroscopy oxybarometer at low fO_2, using both experimental and computational constraints.

To test whether fO_2 buffering can be successful in high pressure experiments, we have carried out a series of experiments with a modified double capsule approach. Because much work has been completed on V valence in glasses across a wide fO_2 range, we can use this information to verify the fO_2 established in the buffer capsule design (Sutton et al., 2005; Righter et al., 2006). We measure the fO_2 of the sample environment within the double capsule using the V-XANES (X-ray absorption near edge structure) K pre-edge peak in glasses of CaO-MgO-Al_2O_3-SiO_2 eutectic composition. After demonstrating the fO_2 environment of the buffer capsule design, we apply this new modified double capsule approach to studying the valence of V in $MgAl_2O_4$ spinels, a common mineral in planetary materials. In particular, we extend V valence studies and V-K pre-edge peaks for spinels from the relatively high oxygen fugacities in Righter et al. (2006) (IW-1 and above) to lower fO_2, where current application of the oxybarometer requires extrapolation. In order to better understand the origin of the pre-edge we also carry out quantum mechanical calculations of the XANES spectra and relate the pre-edge intensity to the material physics. This enables us to know when the barometer can be applied, and under what conditions we may expect deviation from our calibration curve, if any.

Experimental background: control of oxygen fugacity (fO_2)

Experimental comparative studies will be most useful if they are done at a specific and relevant fO_2 for the samples under consideration. At low pressure this can be done by gas mixing or solid buffering (e.g., Mendybaev et al., 1998; McCoy and Lofgren, 1999; Righter et al., 2006), but such experimental systems are usually limited to <1500 °C due to furnace element performance or thermal stability of capsule materials, thus limiting the creation of controlled fO_2 environments at high temperatures.

92 At high pressures, options for controlling fO_2 are more limited as they rely solely on solid
93 buffers. Control of fO_2 in the solid media apparatus (i.e., piston cylinder or multi-anvil) can be
94 achieved using graphite capsules, graphite within Pt double capsule buffering (e.g., Pawley et al.,
95 1992; Righter and Hauri, 1998; Keshav et al., 2004), buffer-doped pressure media (e.g. Dobson
96 and Brodholt, 1999; Rubie, 1999), or the classic double capsule technique (e.g., Huebner, 1971;
97 Ballhaus et al., 1993). Graphite buffers the system at CO_2-CO equilibria resulting in fO_2 values
98 within the range of the terrestrial mantle (FMQ to IW; e.g., Martin and Righter, 2013; Medard et
99 al., 2008; Righter and Hauri, 1998). In the classic double capsule technique, an inner noble
100 metal capsule (typically a metal with high H diffusivity such as AgPd at low temperatures or Pt
101 at higher temperatures) houses the sample material, and a noble metal outer capsule (such as Au
102 at lower temperatures or Pt at higher temperatures) contains a mixture of the buffer components
103 (e.g., metal and metal-monoxide) adjacent to the inner capsule (e.g., Huebner, 1971). Because
104 this technique in theory utilizes known equilibria for any solid buffer desired it can ostensibly
105 extend the achievable fO_2 range to more reducing conditions reflective of the wide range of fO_2
106 recorded in planetary or astromaterials. However, in practice, the classic design is untenable at
107 both low temperatures where buffer material may alloy with noble metal capsules and at high
108 temperatures that exceed the melting point of the capsule materials.

109 Here we describe a new modified double capsule approach that allows fO_2 to be specified
110 across a wide range of values relevant to natural samples. Our approach is a slight modification
111 of previous double capsule geometries, because the outer capsule itself acts as the metal
112 component of the buffer assemblage, and the sample is within a separate ceramic inner capsule.
113 Most of the refractory metal outer capsules tested here – Ni, Co, W, Fe, Mo, V, Cr, Nb, Ta –
114 have high melting points and some even allow experimentation and control of fO_2 to

115 temperatures up to 1900-2000 °C. Coexisting refractory metal and oxide pairs can buffer oxygen
116 fugacity across a wide range of temperatures, and at elevated pressure. In fact, several metal
117 and oxide pairs have been studied together across a wide pressure-temperature (PT) range
118 making them useful buffers in experimental systems (e.g., Ni-NiO and Fe-FeO; Campbell et al.,
119 2009; Co-CoO; Armentrout et al., 2015; W-WO_2; Shofner et al., 2016, Pearce et al., 2010). To
120 illustrate the range possible with some refractory buffers, we calculated fO_2 using
121 thermodynamic data for Re-ReO_2, Ni-NiO, Co-CoO, Mo-MoO_2, Fe-FeO, W-WO_3, Cr-Cr_2O_3, V-
122 V_2O_3, Nb-NbO, Ta-Ta_2O_5, and Si-SiO_2 (**Fig. 1A**). The range of fO_2 defined by these buffers
123 spans the range of fO_2 recorded in natural materials including the Earth, planets, asteroids,
124 meteorites and other astromaterials (**Fig. 1B**; e.g., Righter et al., 2016).
125
126 **Experimental approach**
127 Within our double capsule, the outer and inner capsules each have a specific role, as
128 discussed below. Differences in the reactivities of the buffer assemblages tested here led to
129 slight modifications such that we present here three very similar versions of our modified double
130 capsule design (**Figure 2**).
131 **Outer capsule**
132 In our initial design, the outer capsule is the metal of the buffer, and inside the bottom of
133 the outer capsule is a layer of the oxide portion of the buffer (**Figure 2A**). The inner capsules
134 were nearly a slip fit into the outer metal capsules. Oxide powder was tamped into the very small
135 spaces between the inner and outer capsule walls, and a small amount was sprinkled on top of the
136 inner capsule. In this design, the outer capsule provides structural strength and acts as part of the
137 oxygen buffer if a separate metal is not included inside the outer capsule. Metal-oxide pairs

considered for the initial series were – in order of most oxidized to most reduced – Ni-NiO, Co-CoO, W-WO_2, Fe-FeO, Mo-MoO_2, V-V_2O_3, Cr-Cr_2O_3, Nb-Nb_2O_5 and Ta-Ta_2O_5. The specific capsule material is chosen to minimize reactivity with the inner capsule and sample. A tweak to our initial design uses the classic double capsule technique but with a Mo outer capsule to allow experiments at higher temperatures (**Figure 2B,D**). Finally, NiO and CoO were found to react with or dissolve into Al_2O_3 or MgO inner capsules, and so our third version of the modified double capsule design utilizes a Ni or Co foil to separate these buffers from the inner capsule (**Figure 2C**). See the Results section for a more thorough discussion of these findings.

Inner capsule

The inner capsule is a standard ceramic capsule that contains the sample of interest (**Figure 2**), and provides an inert structure to isolate the sample chemically from the outer capsule. This avoids the formation of buffer oxides within the sample and limits diffusional loss of the sample into the outer capsule. Capsule material could be magnesia (MgO), alumina (Al_2O_3), or graphite as well as other materials. As with the buffer and outer capsule, the specific inner capsule material is chosen to minimize reactivity with the sample. For example, Cr_2O_3 partitions more easily into spinel than Nb_2O_5 (Roeder and Reynolds, 1991; Horn et al., 1994). While the Cr-Cr_2O_3 buffer may be a good choice for buffering fO_2 near IW-5 at 1300 °C, in our studies of $MgAl_2O_4$ spinel described below, Nb-NbO was the buffer employed because the pollution of the spinel component with Nb was minor compared to Cr. The fO_2 of the inner capsule is set by the buffer assemblage in the outer capsule, and can be controlled to low values provided suitable metal/oxide buffer materials are identified that will allow buffering and minimal to no reactivity with the sample composition.

This is the peer-reviewed, final accepted version for American Mineralogist, published by the Mineralogical Society of America.
The published version is subject to change. Cite as Authors (Year) Title. American Mineralogist, in press.
DOI: https://doi.org/10.2138/am-2022-8301. http://www.minsocam.org/

Experimental methods

We carried out two sets of experiments. The first set of experiments tested the buffering capacity of the modified double capsule system, and the second set examined potential changes in V valence in Mg-Al spinels at low fO_2. Within this second set we carried out an additional series exploring the effect of experimental duration to assess equilibrium. Each experiment used a double capsule, was pressurized at room temperature, then heated to run temperature, and finally temperature quenched, as described below.

Experiments utilizing the double capsule

CMAS eutectic glasses. The first set of experiments was designed to produce V-bearing glasses of CaO-MgO-Al_2O_3-SiO_2 (CMAS) eutectic composition (Bowen, 1915) to monitor the fO_2 in the sample environment. The V valence in CMAS glass has been studied previously and is well understood (Sutton et al., 2005). CMAS melt compositions were mixed from oxide powders doped with 1% V_2O_3 and were fused at 1400 °C at FMQ to achieve homogeneity. Fused glasses were ground to a powder and used as starting materials encapsulated in crushable MgO or Al_2O_3 as the inner capsule material. This set of experiments was carried out at 1400 °C and 1 GPa (**Table 1**), with temperature chosen to allow comparison to the 1400 °C V valence calibration of Sutton et al. (2005).

Spinel + V_2O_3 experiments. A second set of experiments examined the valence of V in $MgAl_2O_4$ spinel, with the goal of applying the results to natural systems such as Calcium-Aluminum-rich Inclusions (CAIs) and other small primitive clasts or particles for which standard redox barometers may be absent. Two different variables within the three series of experiments were examined – two at 1400 and 1600 °C utilizing a range of buffers, and one with the Nb-NbO buffer and variable run duration, from 0.5 to 69 hours (**Table 2**). Samples of 99.7 wt% $MgAl_2O_4$

spinel (Alfa-Aesar 99.3 wt% pure) and ~0.3 wt% V_2O_3 (Alfa-Aesar 99.9999% pure), were prepared as homogenized powders. This composition was encapsulated in MgO (partially fused, or magnorite^{TM}, Saint Gobain Ceramics) as the inner capsule material.

Piston cylinder apparatus – 1 GPa experiments[1]. The double capsule samples were loaded into a 13 mm non-end-loaded piston cylinder assembly, with $BaCO_3$ pressure medium, a graphite furnace, with temperature monitored using a Type B or C thermocouple (Righter et al., 2010). Type C thermocouples typically experienced thermocouple failure after 6 hours at 1600 °C, which we attributed to oxidation of the Type C thermocouple (Re-W alloy). Type B thermocouples lasted longer than 6 hours at 1600 °C, thus were used in the time series to enable longer experiments. Samples were pressurized to 1 GPa, heated to the target temperature, and held for the desired length of time before shutting off power and quenching to room temperature. The quench rates were rapid, and typically for this sample assembly and piston cylinder apparatus, temperatures drop to 100 to 200 °C within 2 or 3 seconds, implying quench rates of >500 °C/s.

Analytical methods

[1] Forming spinels at a pressure of 0.5-1.0 GPa significantly simplifies the experimental process but it is worth considering whether it may also alter the geochemical conclusions since we are synthesizing phases that are ostensibly similar to those formed in the solar nebula at pressures < 10^5 Pa. By reference, 1 GPa is a pressure similar to what one may expect from about 30 km of Earth's crust (assuming rho=3 g/cm^3). In the case of spinel, we calculated that 1 GPa of pressure should modify the lattice spacing by about 0.2%. While we acknowledge that this could change thermodynamic values slightly, we assume this contraction in the unit cell is insufficient to cause dramatic alterations in the structure of spinel. A bigger effect is likely to be due to the vapor pressure of phases and subsequent loss, e.g. of Fe, under nebular conditions. However, spinels forming under reducing conditions also tend to be refractory, and the fact that we are able to produce a V-bearing magnesiospinel which exhibits a spectrum similar to natural spinels provides some assurance that the discrepancy introduced is not so large as to modify our conclusions.

Experimental run products were mounted in epoxy, cut, and polished for optical and e-beam imaging and characterization. Micro-sampling of some experimental run products was done using focused ion beam (FIB) techniques. All samples (either using polished mount or FIB section) were characterized using a variety of analytical techniques, including scanning electron microscopy (SEM), electron microprobe analysis (EMPA), synchrotron X-ray microprobe, and transmission electron microscopy (TEM).

The JEOL 7600F field emission SEM at NASA-JSC produces ultra-high resolution electron images with 2-3 nm spatial resolution. The 7600F SEM has two different secondary electron imaging (SEI) detectors and two backscattered imaging (BEI) detectors and an Oxford Symmetry Electron Backscatter Diffraction (EBSD) detector. The Oxford EBSD detector can be used for structural identification of mineral phases, especially when coupled with energy-dispersive X-ray spectroscopy (EDS) spectra. For the EBSD analysis, the sample charges were bisected, mounted in epoxy, and given a mechanical polish with diamond and alumina compound down to 1 μm. The samples were then given a final chemical-mechanical polish with a colloidal silica dispersion to ensure a 50 nm polish was achieved. Once polished, samples were mounted in the SEM and tilted 70° relative to normal incidence of the electron beam at ~18 mm working distance. The grains were imaged using a 10 nA beam current, 20 kV accelerating voltage, and a 1 – 0.5 μm pixel size. The EBSD patterns were indexed based on crystallographic match units from the cubic structure for NbO of Sumin (1989), tetragonal structure for NbO_2 of Arakcheeva et al. (1999) and monoclinic structure for Nb_2O_5 Inorganic Crystal Structure Database #25750 after Anderson (1967). The EBSD data were post-processed using Oxford's Channel5 program suite and orientation maps were produced using the program Tango.

This is the peer-reviewed, final accepted version for American Mineralogist, published by the Mineralogical Society of America.
The published version is subject to change. Cite as Authors (Year) Title. American Mineralogist, in press.
DOI: https://doi.org/10.2138/am-2022-8301. http://www.minsocam.org/

The JEOL JXA-8530F electron probe at NASA-JSC is equipped with 5 wavelength dispersive spectrometers (WDS), a ThermoElectron Silicon Drift Detector (SDD) energy dispersive spectrometer (EDS), and a field emission electron gun which enables significantly improved image resolution. Two of the WDS are high-count-rate detectors that yield detection limits down to 100 ppm for V_2O_5, permitting analysis of trace elements at standard 30 second count times. Metals, oxides, and silicate phases (glass and plagioclase feldspar) were analyzed using a wide range of mineral and synthetic standards (San Carlos olivine, chromite, corundum, hematite, and Ni, Co, W, Fe, Mo, V, Cr, Nb, and Ta metals). Operating conditions were 15 kV, 20 nA sample current, and a point beam (**Table S1**).

The Tescan Vega 3 SEM at the Space Sciences Laboratory, University of California at Berkeley, is equipped with a backscatter detector and an Oxford 80 mm^2 SDD EDS detector and was used for rapid acquisition of quantitative EDS maps. Samples were imaged at various scales with resolution down to ~ 100 nm to locate regions of interest for XANES.

The V valence in glass and spinel run products in polished epoxy mounts was analyzed at the hard X-ray microprobe synchrotron beamline 10.3.2, situated at a bending magnet source at the Advanced Light Source (ALS), Lawrence Berkeley National Laboratory (LBNL). The ALS operates at 1.9 GeV, 500 mA current, and beamline 10.3.2 provides up to 10^9 photons/s at 6 keV. We took 2 μm spatial resolution X-ray fluorescence multi-element maps to select a single phase area, then acquired cumulative V-K edge XANES spectra from one spot (5 x 2 μm). Most areas of the glass run products were completely glassy, and thus the few areas with crystallites near the edges of samples could easily be avoided. The spectra were deadtime corrected, energy-calibrated with a V metal foil standard, and following the method of Sutton et al. (2005), pre-edge intensities were measured relative to the edge jump normalized to 1000. Uncertainty in the

pre-edge peak intensities for samples with a single spectrum (glasses and a few spinels; spnl-Ta and spnl-Cr) is approximately 15%, based on the sum of error in the HWHM and area gaussian fits (glasses and a few spinel samples). Uncertainties for samples for which more than one spectra were obtained are presented as a standard deviation (most of the spinels); typically 2 or 3 points were acquired for each spinel and averages and standard deviations are presented in **Tables 2 and S2.** Because glass and spinel are both isotropic, orientation effects are not an issue as they are with some anisotropic phases (e.g., Sutton et al., 2005; Righter et al., 2006).

The FEI Helios G4 FIB at the LBNL's Molecular Foundry was used to extract thin sections of spinel from the synthetic samples, and the FEI TitanX analytical TEM was used to confirm the crystalline structure of spinel and verify the elemental composition of the spinel phase. EDS maps were acquired at 80 or 200 keV using a Bruker quad SDD on the TitanX in order to verify that V was not present as nano-inclusions (see Supplementary Information, Part 1), and to exclude the possibility that Nb or other buffer materials were present in the spinel at large abundances. Final compositions were derived from off-axis maps, or from precession spectra around a zone axis to remove any influence of electron channeling on the measured composition.

Theoretical Modeling

In order to understand the physics underpinning the oxybarometer, we simulated Vanadium K-edge XANES spectra with pre-edges using the Quantum ESPRESSO (QE) density functional theory (DFT) software suite (Giannozzi et al., 2009, 2017) including XSPECTRA (Taillefumier et al., 2002, Gougoussis et al., 2009). Our simulated spectra include both the dipole and quadrupole interaction – both being important to model pre-edge intensity and shape in the

This is the peer-reviewed, final accepted version for American Mineralogist, published by the Mineralogical Society of America.
The published version is subject to change. Cite as Authors (Year) Title. American Mineralogist, in press.
DOI: https://doi.org/10.2138/am-2022-8301. http://www.minsocam.org/

V-K spectra (Cabaret et al. 2010). We built excited-state pseudopotentials with the Perdew-Burke-Ernzerhof (PBE) exchange-correlation functional (Perdew et al., 1996), using the Atomic code (Dal Corso, 2014) by removing an electron from the 1s orbital and placing it into the lowest unoccupied orbital – the eXcited state Core Hole (XCH) approximation (Prendergast, 2006). Due to known underestimation of strong on-site Coulomb interactions by semi-local exchange-correlation functionals, such as PBE, the calculated electronic structure can overestimate the degree of hybridization between transition metal atoms and ligands resulting in unrealistic electron delocalization. This can lead to degraded spectral fidelity and incorrect band gaps. The Hubbard U (DFT+U) correction (Anisimov et al., 1997; Gougoussis et al., 2009) is designed to enhance localization of electronic structure due to string on-site Coulomb interactions, controlled by the on-site energy U, which penalizes delocalization of electrons. We applied such corrections for two of our systems and used +U values for the 3d orbitals (**Table S3**) from Wang et al. (2006) and Capdevila-Cortada et al. (2016). We carried out the simulations using the compute clusters at the LBNL Molecular Foundry and ALS. We created crystal structures with the aid of CrystalMaker (Palmer, 2015), and Atomsk (Hirel, 2015), and also used Quantum Vitas as a productivity and analysis aid (Huang, 2020) as well as fityk (Wojdyr, 2010), and our own scripts written in python (Gainsforth, 2020).

We simulated XANES spectra for several spinels with compositions representative of known oxidation states and compositions pertinent to our synthesis runs. All simulated phases are shown in **Table S3**. Our $MgAl_2O_4$ model is a pure $MgAl_2O_4$ with a single vanadium atom which mirrors the composition of spinel synthesized in this paper (Spinel-V-008 **Table 2**). The magnesiochromite model is a chromite-rich spinel matching the composition of a spinel formed at fO_2 = IW-1 (from Table 2 of Righter et al., 2006). The Fe_3O_4-rich model matches a spinel

formed at fO_2 = IW+7.6 (202 in Table 2 of Righter et al., 2006). These three spinel compositions were selected because XANES spectra were collected from the experimental samples, which will be compared to the simulated spectra in the results section below. We also carried out several simulations matching compositions that we did not synthesize but which demonstrate how spectra change in response to variation in crystal composition. These are labeled 1% Fe Tet, 1% Fe Oct, 1% Cr, 1% Ti, 2% Ti and Chromite in **Table S3** and are explained below.

We used a 2x2x2 supercell (a=b=c=11.555Å, a=b=c=60°of the spinel primitive unit cell with a total of 112 atoms including 32 octahedral cations and 16 tetrahedral cations (**Figure 3)**. For spinels with complicated compositions, we placed atoms at random within the constraints: 1) the total cell composition must match the expected composition, 2) atoms may only be placed in sites that preserve the known oxygen stoichiometry. For example, Cr must occupy an octahedral site. The positions of the atoms and the lattice parameter of the unit cell were allowed to change in order to minimize the energy. We then carried out XSPECTRA calculations of the V-K edge.

We processed the theoretical spectra as in Sutton et al. (2005) in order to estimate the expected V-K pre-edge amplitude as a function of the crystal composition. We simulated edges using both the dipole approximation, and the quadrupole approximation because it has been postulated that the dipole pre-edge intensity should be suppressed when the V-O_6 octahedron is highly symmetric (Cabaret, et al., 2010).

Calculation of fO_2 from the buffered experiments (databases and results)

Calculations of fO_2 were straightforward for most of the buffers used, where the metal and oxide phases were present and thermodynamic data available across the temperature range of

interest and relevance. For example, Gibbs free energy data from Barin et al. (1995) was used to calculate fO_2 for the buffers Ni-NiO, Co-CoO, Mo-MoO_2, W-WO_2, Fe-FeO, Cr-Cr_2O_3, V-V_2O_3, Ta-Ta_2O_5 and Si-SiO_2 across a wide temperature range (**Table S4**). Data from Pownceby and O'Neill (1994) were used for Re-ReO_2. In modeling of equilibria involving tungstates, niobates, and chromates, thermodynamic data were utilized from various sources: Mg_2WO_4 data is from Raghavan and Kay (1990), $MgCr_2O_4$ data is from Robie et al. (1978) and Klemme and O'Neill (1997), and $MgNb_2O_6$ data (estimated from the oxides MgO and Nb_2O_5) as well as the buffer Nb-NbO utilized thermodynamic data from Jacob et al. (2010) and Raghavan (1991). For a general metal–oxide equilibrium reaction such as $M + x/4\ O_2 = MO_{x/2}$ (where x is the valence of the metal oxide), the fO_2 is related to the Gibbs free energy (G°) by the following equilibria:

$$\Delta G^\circ = -RT\ln K$$

(where R is the gas constant, T is temperature in Kelvin and K is the equilibrium constant)

$$-\Delta G^\circ/RT = \ln[(aMO_{x/2})/(fO_2)^{x/4}(aM)] = \ln(aMO_{x/2}) - x/4\ \ln(fO_2) - \ln(aM)$$

Because $aMO_{x/2}$ and aM are both unity for a buffer, this simplifies to:

$$-\Delta G^\circ/RT = -\ x/4\ \ln(fO_2) \quad \text{or} \quad 4\Delta G^\circ/xRT = \ln(fO_2) \text{ or } \quad fO_2 = \exp\ (4\Delta G^\circ/xRT).$$

Where fO_2 is displayed relative to the iron-wüstite buffer (IW), we normalized the absolute value of $\log(fO_2)$ to that at the Fe-FeO buffer at the same temperature using data from Barin (1995). At 1400 °C, the range of relative fO_2 covered is from IW+4.5 to IW-6.5; the temperature dependence of most buffers is weak so the range of values at 1600 °C is very similar.

Results

Characterization of the experimental buffers

Verification of the buffers was done by SEM, EMPA and EBSD (**Figures 4 and S1**). SEM imaging was used to document the textures, EMPA was used to confirm stoichiometry of the oxide phases and the overall composition (and purity) of the metal and oxide buffer phases, and EBSD was used to identify and/or confirm mineral structures in cases where there was uncertainty.

For most experiments, the buffer metal and oxide were intact after an experiment, and clearly separated from the sample capsule and the sample. For example, the experiment with the Ta-Ta_2O_5 buffer (**Fig. 4A**) had a ~100 μm thick layer of Ta metal and Ta_2O_5. However, as will be described below, several issues — expiration of the buffer, reactivity, capsule solubility, and phase transformations — required slight design changes to maintain the buffers as desired.

Some of the reduced buffers experienced expiration of the oxide phase and thus required a slight modification of the double capsule design. These reduced buffers (Ta, Nb and Cr; **Fig. 4A-4C**) were successfully employed by using the classic double capsule technique but with an outer Mo capsule, which enclosed a mixture of the buffer metal and oxide at the bottom of the outer capsule, to avoid issues of capsule melting at high temperature or alloying with the buffer material. With this configuration, the metal-oxide pair was maintained throughout the experiment, rather than one or the other being exhausted.

In some experiments, the buffer metal or oxide reacted with the assembly components such as the Al_2O_3 inner capsule or the MgO capsule material to form aluminates, tungstates, molybdates, niobates, and chromites (see section below on the buffering capacity of the double capsule environment) (**Fig. 4C-4E**).

In initial experiments with Ni and Co buffers, the NiO and CoO dissolved into the MgO capsules thus exhausting the oxide portion of the buffer. Thus, it was unclear if these

359 experiments were maintained at a buffer, and in fact some early results indicated that the fO_2
360 imposed was not as oxidized as expected. To circumvent this issue, Ni or Co metal foil discs
361 were used to separate the NiO and CoO from the MgO capsule surface in order to minimize the
362 direct solubility of the buffer oxide into the MgO (**Figure 2C**), and thus promote the stability of
363 the pure buffer oxide phases – NiO or CoO. All Ni-NiO and Co-CoO buffered experiments
364 reported in **Table 1** utilized this configuration. At reducing conditions imposed by the V, Cr,
365 Nb, and Ta buffers, an additional concern is the solubility of the metal buffer into Fe metal. We
366 observed Fe-V alloys in experiments carried out with the V-V_2O_3 buffer and because we are
367 studying V in spinel we decided not to use this buffer to eliminate the second source of V. Phase
368 diagrams for Fe-Nb and Fe-Ta show that solubility of Fe into the buffer metal will be minor with
369 no more than 5 wt% Fe dissolving into the metal (Okamoto, 1990). This will not have a
370 substantial effect on the buffering ability. The Fe-Cr system however, is more similar to the Fe-
371 V system and thus significant alloying of Fe with Cr metal may affect the buffer integrity in Fe-
372 bearing systems (Okamoto et al., 1990). This could be mitigated by using known activity-
373 composition relations for the Fe-Cr system.

374 Finally, the Nb experiments exhibited an unusual texture and oxide phase with a Nb:O
375 stoichiometry of 1:1, not 2:5 as expected from the starting materials. Examination of this phase
376 by EBSD confirmed the cubic structure expected of NbO, and not the orthorhombic, monoclinic,
377 or tetragonal associated with Nb_2O_5 (**Fig. 5**). The niobium oxide buffer material consists of
378 intergrowths of cubic NbO and tetragonal NbO_2 which are both well indexed by EBSD with
379 average mean angular deviation values for each phase < 0.7. The intergrowths consist of skeletal
380 grains of cubic NbO included in massive grains of tetragonal NbO_2 (**Fig. 5**). Therefore, oxygen
381 fugacity was computed using the Nb-NbO buffer in these cases.

This is the peer-reviewed, final accepted version for American Mineralogist, published by the Mineralogical Society of America.
The published version is subject to change. Cite as Authors (Year) Title. American Mineralogist, in press.
DOI: https://doi.org/10.2138/am-2022-8301. http://www.minsocam.org/

382

383 **Experimental and analytical results for glasses**

384 The diopside-anorthite eutectic melt reacted in some cases with the alumina capsule, and
385 thus the overall sample composition gained Al_2O_3 from the capsule. However, this reaction
386 stabilized plagioclase feldspar (**Fig. 4B**) which has higher Al_2O_3 content than the glass and so the
387 glass compositions in these melts stayed very similar to the glass compositions in MgO capsules
388 (**Table S1**). In addition, in most cases the CMAS liquids dissolved small amounts of oxide from
389 the buffer material such as CoO, WO_3, Nb_2O_5, and MoO_2 (**Table S1**) into the silicate melt.
390 Glasses contain 0.35 to 0.40 wt% V_2O_3, whereas the plagioclase contained V below detection
391 limits, consistent with the incompatibility of V measured by Bindemann et al. (1998). V XANES
392 spectra of the CMAS glasses exhibit pre-edge peaks associated with V^{3+} (Sutton et al., 2005;
393 Righter et al., 2006). Pre-edge peaks for the glasses in this study occur between 5467-5469 eV
394 (**Fig. 6**).

395

396 **1400 °C and equilibration of spinels**

397 Experiments with $MgAl_2O_4$ spinel and V_2O_3 reacted to form V-bearing $MgAl_2O_4$. Most
398 textures are homogeneous with some exhibiting triple junction boundaries where they have re-
399 crystallized (**Fig. S1**). Rarely some impurities or a V hotspot are observed, but these
400 experimental runs also contained the V-bearing $MgAl_2O_4$ spinel on which we are focused (e.g.,
401 Supplementary Information, Part 1). XANES K edge spectra of V_2O_3 and $MgAl_2O_4$ spinel are
402 distinct, especially in the EXAFS region (**Fig. S2**) and thus could also be used to verify that the
403 V was sited in spinel and not in a V-rich hotspot such as V_2O_3, for example. Experiments with
404 the V-V_2O_3 buffer in the double capsule resulted in V mobility into the sample capsule as well,

405 producing a gradient of V concentrations, and thus zoning of V in the spinels. These
406 experiments are not used in the assessment. Buffers in the spinel series remained intact, and in
407 the case of the Cr buffered sample the Cr_2O_3 reacted with MgO to form some $MgCr_2O_4$ as well
408 (**Fig. S1**). Spinels in this series contained between 0.1 and 0.4 wt% V (**Table S5).** Spinels from
409 1400 °C experiments exhibited more V compositional variation, suggesting that the 1400 °C
410 experiments did not approach equilibrium. Diffusion data for V in chromite are not available, but
411 sluggish kinetics are expected based on available diffusion data for spinel structured oxides;
412 diffusion of Cr in spinels is known to be slower than for Mg (e.g., Suzuki et al., 2008; Sheng et
413 al., 1992; Sievwright et al., 2020). If V exhibits similar diffusivity to Cr, there may be kinetic
414 barriers to equilibration or re-equilibration in spinels even at these high temperatures.

415 V XANES spectra for all 1400 °C spinels exhibit small pre-edge peak intensities and
416 energies that are representative of reduced vanadium as expected (**Fig. S3**). However, because
417 V_2O_3 was added to the starting materials and it is possible that there was a kinetic barrier to re-
418 equilibration we carried out a series of experiments at higher temperatures, including runs of
419 variable duration in order to mitigate slow kinetics and disequilibrium.

420

421 **1600 °C results and discussion – Cr, Ta, Nb and time series**

422 Higher temperature experiments were completed both to ensure a close approach to
423 equilibrium, and to synthesize spinels at reduced conditions where V^{3+} and V^{2+} are thought to be
424 stable (e.g., Paque et al., 2013; Righter et al., 2006). An initial series at the Nb-NbO buffer (IW-
425 5.44) investigated the effect of experimental duration on the buffer integrity, the spinel
426 composition, and the valence or pre-edge peak intensity. This reduced buffer Nb-NbO was
427 chosen to encourage V^{2+} stability to the greatest extent possible. Runs of shorter duration (<1

hour) exhibited textural dis-equilibrium with finer grain sizes and many phases adjacent to the spinels indicating incomplete equilibrium. Runs of longer duration (>1 hour) exhibited coarser grain size, grain boundaries of ~120° triple junctions (equidimensional grains), inclusion-free interiors (e.g., **Figure 7C**), and yielded the same phase assemblage which indicates the reproducibility of the results. The latter were selected as locations for EMPA and XANES analyses of the spinels. Some of the longer duration spinel samples were also infiltrated by MgNbO phases along grain boundaries – these mobilized from the buffer material but did not affect the overall composition of the spinel, which contained only Mg, Al, O, and V, as expected. The other reduced experiments at the Ta-Ta_2O_5 and Cr-Cr_2O_3 buffers also contained homogenized spinel. BSE images reveal some local areas of heterogeneity that likely represent impurities from the $MgAl_2O_4$ starting materials (e.g., Ca), but overall exhibit clear spinel areas with equilibrated textures and grain boundaries (**Figures 7A,B**).

The reduced 1600 °C spinel samples also exhibited small V XANES pre-edge peaks (**Figure 8**), with no obvious correlation with run duration. No discernable difference in the spinels of variable duration up to 70 hrs. indicates that V valence equilibrium was approached in these high temperature experiments. Additional experiments using the Cr-Cr_2O_3 (IW-3.51) and Ta-Ta_2O_5 (IW-5.37) reduced buffers at 1600 °C also showed small pre-edge peaks with intensities consistent with reduced vanadium. For comparison to the reduced spinel spectra, **Figure 8** also includes V XANES spectra from a magnesiochromite at IW-1 and a magnetite synthesized at IW+7.6, both synthesized by Righter et al. (2006). The magnesiochromite pre-edge peak is nearly identical in magnitude and energy to the reduced spinel from the present study, while it is only at the higher fO_2 and magnetite spinel composition where the pre-edge peak become more intense (**Figure 8**) as expected from the Righter et al. (2006) oxybarometer.

This is the peer-reviewed, final accepted version for American Mineralogist, published by the Mineralogical Society of America.
The published version is subject to change. Cite as Authors (Year) Title. American Mineralogist, in press.
DOI: https://doi.org/10.2138/am-2022-8301. http://www.minsocam.org/

The results from all of these series together indicate that spinels from our highest temperature, most reduced conditions, and with the most equilibrated textures, exhibit small pre-edge peaks – similar in magnitude to those measured in previous experiments at IW-1 (Righter et al., 2006; **Figure 8**), and also indicate that the pre-edge peak intensity correlation with fO_2 at conditions < IW-1 might be non-linear.

Observed pre-edge characteristics and intensities from DFT modeling

Simulated spectra for V-bearing spinels can reproduce the experimental spectra for the Fe_3O_4-rich spinel and for the $MgAl_2O_4$ end member (e.g., **Figure 9)**. **Figure 9A** shows a comparison of the experimentally acquired $MgAl_2O_4$ spectrum (blue), taken from the sample Spinel-V-008, run E-117 (**Table 2**), with two DFT modeled spectra. The first simulation is convolved with a small, 200 meV Gaussian so that it shows the predicted spectral features (shown in green). In the second case it is convolved with a larger 1.8 eV Gaussian in order to smooth the simulation to better reproduce the experimental spectrum. A small pre-edge can be seen at 5468 eV in the theoretical spectrum or 5466 eV in the experimental spectrum.

In **Figure 9B**, theoretical pre-edges for several different compositions are shown. The Fe_3O_4-rich spinel was sensitive to DFT+U and is plotted with and without a +U energy correction. DFT+U can be important for capturing the splitting and exact positions of the spectral features within the pre-edge correctly. However, the +U correction only changed the pre-edge intensity by ~10%, and the correction had no effect on the $MgAl_2O_4$ spectrum. Therefore, we deem DFT+U a second order correction for these compositions, though it may remain important for other compositions.

Our modeling reproduces the experimental trend qualitatively – namely that spinels which form at lower oxygen fugacity have less intense pre-edges. However, the modeled intensities can be substantially offset from the experimental values in important cases (**Figure 9C**). DFT predicts a pre-edge intensity (as a fraction of the edge-jump = 1000) of 87 for $MgAl_2O_4$ whereas the experimental value is 18. To investigate this discrepancy, we modeled the effect of chemical composition on the Vanadium pre-edge intensity as follows. Because our simulated unit cell has 112 atoms, replacing a single site with a transition metal is approximately equivalent to adding 1 at% of that chemical species to pure $MgAl_2O_4$. We created 5 theoretical spinel compositions to explore the effect of other transition metals on the pre-edge intensity. In the simplest composition, $MgAl_2O_4$ contained only a single V atom substituting for Al. For the other compositions, we added one additional atom: tetrahedral Fe (Fe^{2+}), octahedral Fe (Fe^{3+}), octahedral Cr (Cr^{3+}), and octahedral Ti (Ti^{3+}). The octahedral substitutions were done to the same site 4.986 Å from the V, while the tetrahedral substitution was 5.307 Å. In the case of Ti, a second 2% Ti composition was used with an additional octahedral Ti atom 8.661 Å from the V site. Each is close to end-member $MgAl_2O_4$, but the pre-edge intensity varies by a factor of 4x (**Table S3**).

In order to disentangle the spinel composition from the derived oxidation state of V, we calculated the spin structure of the V impurity. A neutral V atom has an electron configuration of $[Ar]3d^3 4s^2$. In the $MgAl_2O_4$ spinel model we found two spin-up electrons in the V-3d shell, and an empty 4s shell, which implies a 3+ oxidation state, which is consistent with the higher predicted pre-edge intensity for this structure than the observed experimental pre-edge intensity. When we calculated the V spin structure of the $MgAl_2O_4$ spinel with small amounts of Ti in addition to V, we found Ti^{3+} and V^{3+} to be present, but now the predicted pre-edge intensity was

lower, in agreement with the experimental spinels. Such spinel compositions commonly occur in meteoritic samples formed under very reducing conditions, e.g. in CAI's (Paque et al., 2013; Connolly et al., 2003) and in Al-rich chondrules (Jilly-Rehak et al., 2017).

We plotted the single-electron wavefunctions contributing to the pre-edge peak and found the surprising result that they are strongly hybridized between all the transition metals in the crystal. That is, the V-K pre-edge structure is not, in fact, only due to the hybridization of V 3d electrons with the p-orbitals of neighboring oxygen atoms, but also largely due to the hybridization of V 3d electrons with 3d electrons from neighboring Ti, Fe, and Cr atoms. The number and location of other transition metals has a significant effect on the pre-edge intensity. We will explore the reason for this, and the implications for the oxybarometer in the discussion.

Discussion

Buffering capacity of the double capsule and the CMAS glass experiments

The V-K XANES pre-edge peaks were used to calculate effective V valence (V*) and also fO_2 (Righter et al., 2006; Sutton et al., 2005) using the normalized pre-edge peak intensities (I) (**Fig. 10 and Table S2**). The expression from Sutton et al. (2005):

$$I = -153+199(V^*)-106(V^*)^2+2.4(V^*)^3,$$

was used to calculate the V* for each glass. Pre-edge peak intensity and the calculated V* for the glasses generally correlate with the fO_2 calculated for each buffer over a wide range, but the correlation is poor (Figure S3) with $R^2 = 0.556$. This poor correlation was not anticipated and it was hoped that the V glass oxybarometer would be a useful and elegant way to establish fO_2 in the double capsule assembly. However, the poor correlation is most likely attributable to extrapolation of the oxybarometer into more reduced conditions than its calibration and to

519 compositional variation in the glasses. We also considered oxybarometer pressure dependence,
520 quench rates and coupled redox change, and beam damage from high photon flux densities, but
521 these effects are relatively small and insignificant compared to the calibration and compositional
522 variation (see Supplementary Information, Part 2, for a more detailed discussion).

523 To constrain the oxygen fugacity in the double capsule assemblies employed, we instead
524 examine the secondary phase equilibria established in many of the experiments. These equilibria
525 involved metal and oxides for which thermodynamic data are available, and therefore can be
526 used to calculate the fO_2 within the assemblies. In some experiments, Ni and Co reacted with the
527 Al_2O_3 inner capsule to form a thin layer of $NiAl_2O_4$ and $CoAl_2O_4$ spinel at the interface between
528 the metal and alumina, according to the following two equilibria:

529 $Ni(s) + Al_2O_3(s) + ½\ O_2(g) = NiAl_2O_4(s)$

530 $Co(s) + Al_2O_3(s) + ½\ O_2(g) = CoAl_2O_4(s)$

531

532 Similarly, some buffer metals or oxides reacted with the MgO capsule material to form
533 additional phases such as Mg_2CrO_4, $MgMoO_3$, $MgNb_2O_6$, and Mg_2WO_4 (**Fig. 4C-4E**). In some
534 of these cases, the original oxide buffer material was lost or contaminated, but the formation of
535 new phases still permitted calculation of fO_2 according to the equilibria:

536 $Cr(s) + 2MgO(s) + O_2(g) = Mg_2CrO_4(s)$

537 $2Nb(s) + MgO(s) + 5/2\ O_2(g) = MgNb_2O_6(s)$

538 $W(s) + 2MgO(s) + O_2(g) = Mg_2WO_4(s)$

539 and

540 $Mo(s) + MgO(s) + O_2(g) = MgMoO_3.\ (s)$

The Cr, Ni, and Co equilibria were used to calculate log fO_2 using thermodynamic data from Robie et al. (1978), Nb equilibrium was used to calculate log fO_2 using thermodynamic data from Jacob et al. (2010), W equilibrium was used to calculate log fO_2 using thermodynamic data from Raghavan and Kay (1990), and Mo equilibria was used to calculate log fO_2 using thermodynamic data from Morishita et al. (2018). The oxide phases formed - $NiAl_2O_4$, $CoAl_2O_4$, Mg_2CrO_4, $MgNb_2O_6$, Mg_2WO_4, and $MgMoO_3$ - were all nearly pure (e.g., **Table S1**); for the calculations, mole fractions and activity coefficients were assumed to be unity.

Comparison of the expected fO_2 from the buffer and the fO_2 calculated from these equilibria show very good agreement across a wide range of fO_2 from values of ~ -16 to -6, or 10 log fO_2 units (**Figure 10**; $R^2 = 0.933$). This indicates that the buffers are indeed imposing a specific fO_2 in the environment, and that this experimental design can be used to study a wide range of fO_2 with the use of the buffers employed here. The piston cylinder sample environment is known to be a relatively open system, with H_2 passing easily through the solid media and ceramic spacers and capsules via H_2 diffusion (e.g., Brooker et al., 1998; Matjuschkin et al., 2015). If robust redox equilibria are established within this double capsule geometry, fO_2 is imparted to the sample environment as long as the buffering phases are intact. Our experiments at 1600 °C with Nb-NbO buffers (or Nb-Niobate equilibrium) intact after 70 hours indicate buffering can occur even at these high temperatures and long duration to study many equilibria – even with sluggish kinetics – with ample time to promote equilibrium. The intact buffers and evidence for equilibrium presented above thus strongly support the growth of the spinels in this study at the intended oxygen fugacities.

V valence in $MgAl_2O_4$ spinels

564 The use of V valence in spinels as an oxybarometer has been studied for chromian spinels
565 and magnetites at oxygen fugacities above IW-1 (Righter et al., 2006; Toplis and Corgne, 2002).
566 Righter et al (2006) demonstrated a shift in pre-edge peak intensity and energy that correlates
567 with average V valence (V*) and fO_2; V-K XANES pre-edge peaks shift from high energies and
568 intensities (5470 eV and 600, respectively) at oxidized conditions near the hematite-magnetite
569 (HM) buffer to lower energies and intensities (5467 eV and 50, respectively) at more reducing
570 conditions near the IW buffer. This relationship between V* and fO_2 was approximately linear,
571 but spinel was offset below the glasses by approximately one valence unit (Righter et al. 2006).
572 From this previous work, the expectation is that if V^{4+} was stable in spinels equilibrated at the
573 oxidized conditions (e.g., Ni-NiO and Co-CoO buffers), the pre-edge peaks would be higher and
574 peak energies shifted to 5470 eV (Righter et al., 2006). If V^{2+} is present in spinels equilibrated at
575 the reduced Cr-Cr_2O_3, Ta-Ta_2O_5 and Nb-NbO buffers, the pre-edge peaks would be lower and
576 shifted to lower energies, as might be expected if V^{2+} had a pre-edge intensity of zero. Indeed,
577 pre-edge peaks in natural spinels from reduced meteorites such as lodranites (Righter et al.,
578 2016) or from chondrules (Jilly-Rehak et al., 2017) have normalized intensities near or below 30,
579 which was taken to imply the presence of some fraction of V^{2+}.

580 The desire to extend the Vanadium oxybarometer to lower fO_2 conditions has been
581 limited by availability of experimental data to mostly oxidized conditions (> IW-1 in Righter et
582 al., 2006), and the practical challenges associated with producing reducing conditions in
583 experiments at high temperatures. Our high pressure solid media experimental approach is thus
584 ideal for addressing this need for Vanadium K-edge measurements at reducing conditions to
585 better constrain the extended oxybarometer. The expectation of finding V^{2+} was not realized in
586 our experiments - even the most reduced experiment products had measurable pre-edge peaks

that are associated with V^{3+}. This lack of evidence for V^{2+} in the most reduced spinel motivated DFT calculations to explore possible causes of this behavior.

$MgAl_2O_4$ + V theoretical structure

While DFT modeling was able to reproduce the low pre-edge intensities that correspond to V* < 3 values at low fO_2, the results of spin structure analysis suggested that the oxidation state was in fact V^{3+}, and additional cations Ti, Cr or Fe were necessary to suppress the predicted V pre-edge intensity to match experimentally acquired spectra. Therefore, we find that V* can be used only as a proxy for fO_2 and not for deriving the oxidation state of V in spinel. The prevalence of V^{3+} in all of the reduced, high temperature equilibrated spinel experiments suggests that the aluminous spinels are more selective than other spinel structures and show a strong site preference for V^{3+}. This lack of dependence on V valence with fO_2 at <IW-1 is consistent with two other independent studies examining V valence in aluminous spinels. Paque et al. (2013) found no evidence for variable valence in aluminous spinels in CAIs which equilibrated at solar nebular fO_2 (IW-4 to IW-6); all spinels were measured V* ~ 2.5. Bosi et al. (2016) found no evidence for V^{4+} in aluminate spinels, even at high oxygen fugacities where V^{4+} is stable in magnetites and Fe-Ti spinels (e.g., Righter et al., 2006). This indicates that the accommodation of specific V-valences can be strongly influenced by structural constraints of the crystal lattice. V^{4+} may thus be excluded from aluminous spinels at high fO_2 (e.g., Toplis and Corgne, 2002; Balan et al., 2006), and V^{2+} largely excluded at low fO_2. Chromian spinels of Righter et al. (2006) show large variation in V valence that may be attributed to Ti, Fe^{3+}, and Cr making more site opportunities for V^{4+} compared to an aluminous spinel. The V* = 2.5

609 measured in CAI spinels of Paque et al. (2013) and Connolly and Burnett (2003) may have been
610 stabilized by the presence of other cations in those natural spinels.

611 Furthermore, while simulation of V-K in almost-pure $MgAl_2O_4$ produced a pre-edge
612 intensity 4x as large as we experimentally measured, the addition of a small amount of
613 tetrahedral Fe, or octahedral Ti or Cr, suppresses the pre-edge peak intensity and thus brings the
614 theoretical intensity in line with experimental values. V-bearing magnesiospinels indeed have
615 some small amount of these other elements when they form under natural conditions. The effect
616 of multiple cations on the V-K pre-edge may be probed by their contributions to the band gap.
617 The band gap in $MgAl_2O_4$ is 7.8 eV (Borges et al., 2016, French et al., 1989). We computed a
618 band gap of 5.2 eV which aligns with similar DFT calculations from literature, where the
619 underestimate is expected for DFT calculations which do not include higher order corrections for
620 multi-particle interactions (Begum et al., 2021). The inclusion of transition metal impurities such
621 as octahedral V and Ti introduces charge states in the middle of the band gap, where the states
622 responsible for generating the pre-edge are about 1 to 1.5 eV below the lowest conduction band
623 (if they produce empty states which obey optical selection rules). Therefore, we expect the
624 intensity and positions of pre-edge peaks to be strongly dependent on the exact chemistry of
625 these impurities: that is, V-Ti impurity pairs formed at the same oxygen fugacity as V impurities
626 may yet show different spectral characteristics since the pre-edge is formed by states produced
627 by both impurity elements.

628 **Figure 11A** shows a Bloch wave projection for the states contributing to the V-K pre-
629 edge in pure $MgAl_2O_4$. These states have x^2-y^2 and z^2 character localized around the V atom –
630 meaning it only hybridizes significantly with its neighboring oxygen octahedron. **Figure 11B**
631 shows a similar projection for V with two Ti atoms also in the unit cell. While the orbitals are

still primarily d-orbital in character, the two Ti atoms have taken much of the charge density away from the V atom which weakens the pre-edge transition intensity, and dramatically changes the symmetry of the overall Bloch wave. In addition, the position of the Fermi level in pure $MgAl_2O_4$ is well below the orbitals which indicates that they should be empty and able to accept transitions. The Ti-bearing spinel, by contrast, has brought the orbitals to the Fermi level which indicates that they will be filled and unable to accept transitions. We therefore see two important effects: 1) Ti redistributes the charge relative to the V atom and changes the Fermi level which weakens the intensity of this transition, and 2) the symmetry is broken which can enable the dipole intensity relative to the quadrupole intensity. It is therefore very important to include the quadrupole contribution as noted by Cabaret et al. (2010) but because of the large number of configurations possible, it is non-trivial to predict whether the dipole or quadrupole will be dominant without executing the full simulation.

As the density of impurities increases, the number and energy separation of pre-edge states increases. In the limit of a spinel vastly enriched with transition metals it becomes a conductor, e.g. magnetite (Fe_3O_4) is a conductive spinel. We were able to correctly simulate the pre-edge structure for the two limiting cases: an insulator consisting of pure $MgAl_2O_4$ with minor impurities and a conductor consisting of Fe_3O_4-rich spinel. However, since DFT systematically underestimates the band gap unless computationally prohibitive corrections are added, there is a range of compositions which are enriched in transition metals but which are still insulators that we cannot currently simulate. Our DFT simulation models them as conductors and overestimates the pre-edge structure, which we suggest is the reason for the poor match between simulated and experimental pre-edge intensities for the magnesiochromite composition (**Figure 9C**).

On this basis, we conclude that oxidation state alone is insufficient to explain pre-edge intensity, but since our simulations show that realistic compositions do in fact manifest the hypothesized correlation between pre-edge intensity and fO_2 during formation, we explore the bounding conditions where we can still use the oxybarometer.

As a new hypothesis, we first observe that the mineral composition is largely determined by fO_2 during formation. Typical bulk compositions found in nature that form spinel at higher fO_2 enable cations to enter the crystal, which change the number and symmetry of states accessible in the V-K XANES pre-edge as shown above. Depending on the exact compositions, and which sites the cations occupy, this can both suppress or increase pre-edge intensity depending on the effect of the hybridization between the V center and additional cations. In the limiting case that the spinel is conductive, we expect that the large number of states just above the Fermi level provide a significant boost to the pre-edge intensity. The exact mechanics of this bear further study, but for the purpose of this paper we simply note that the hybridization between the V-d orbitals and M-d orbitals (M are other transition metals) leads to important interactions that change the pre-edge intensity in a significant way.

In the low fO_2 regime, cations such as Fe and Cr are typically not favored for entering spinel whereas Ti can -- and we found that Ti in small concentrations will suppress the pre-edge structure. In retrospect, we can also see the influence of Ti in previous experiments. Righter et al. (2006) synthesized five spinels near the FMQ buffer but with different bulk compositions where V and Ti varied up to 10% of the bulk composition. The V-K pre-edge intensities for the Ti-enriched spinels were 45 and 50, whereas the V-rich spinels had pre-edge intensities of 102 and 165, even though the fO_2 were all within a ½ log unit of each other, and the Ti-rich composition actually formed at higher oxygen fugacity yet had a suppressed pre-edge. Righter et

This is the peer-reviewed, final accepted version for American Mineralogist, published by the Mineralogical Society of America.
The published version is subject to change. Cite as Authors (Year) Title. American Mineralogist, in press.
DOI: https://doi.org/10.2138/am-2022-8301. http://www.minsocam.org/

al. (2006) also synthesized a set of 5 spinels near the IW buffer and found a similar phenomenon: the Ti-enriched specimens had half the V-K pre-edge intensity compared to the V-rich specimens despite forming at the same fugacity.

Clearly, the pre-edge intensity is not only a function of oxygen fugacity but also of bulk composition. However, for natural spinels which form from similar bulk compositions, the oxybarometer should hold. Whereas, for bulk compositions too distant from common geological systems, containing a-typical elements (e.g. Sr, or excess Ti) it may be possible to break the oxybarometer. In those cases, the competition for elements between phases will be significantly different and could override the dominance of oxygen fugacity. An example of this can be seen in our theoretical simulation where octahedral Fe increases the pre-edge intensity in $MgAl_2O_4$ but tetrahedral Fe reduces it. Within natural geological settings, one or the other will always be thermodynamically favored, and in the case of fO_2 < IW-3, tetrahedral Fe^{2+} will be favored which implies a diminished V-K pre-edge.

Barometers based on pre-edges of other elements in spinel (or any other phase, presumably) should show similar compositional dependencies. For example, the pre-edge intensity of Ti-K in $MgAl_2O_4$ is likely to be influenced by the presence of V, whether or not the formal oxidation state of Ti changes.

fO_2 vs pre-edge intensity in spinel

Ideally, we wish to be able to determine the fO_2 during spinel formation using only the intensity of the V-K XANES pre-edge. However, we learned that a perfect relationship does not exist because the pre-edge intensity is influenced by the bulk composition as well as fO_2 during formation. Nevertheless, the strong correlation plotted in **Figure 12A**, combining new and

This is the peer-reviewed, final accepted version for American Mineralogist, published by the Mineralogical Society of America.
The published version is subject to change. Cite as Authors (Year) Title. American Mineralogist, in press.
DOI: https://doi.org/10.2138/am-2022-8301. http://www.minsocam.org/

previous data, from Righter et al. (2006), tells us that fO_2 can still be constrained. The previous work recognized that crystal chemistry influenced pre-edge intensity but attributed the spread of pre-edge intensities at a given fugacity as statistical uncertainty -- i.e. an experimental error rather than systematic differences in composition requiring separate treatment. We now recommend treating the spread as a real effect of uncertainty in the "measured" oxygen fugacity. For example, depending on the composition of a given spinel crystal, it could be possible to interpret a pre-edge intensity of 100 anywhere from IW up to IW+6 (Fig 12A).

While this dissatisfying result is strictly correct, it is possible to do better by utilizing information about the composition of the spinel -- information which is typically available to the experimentalist. We propose a calibration to predict the oxygen fugacity at which a spinel formed based on the pre-edge peak intensity (I_{pre}), the pre-edge peak position in eV (E_{pre}) and the atom% of Mg and O:

$$\Delta IW = 4.35e\text{-}3\ I_{pre} + 2.55\ (E_{pre}\text{-}5469) + 0.253\ Mg - 1.05\ O + 57.7$$

We find this calibration improves the predictive value across the entire range of fO_2 making it possible to predict a fugacity within a few log units irrespective of composition. This is shown in **Figure 12B**.

Implications

We demonstrate that the solid buffering approach introduced here applies a specific fO_2 to the sample environment, as sensed and measured using metal-oxide equilibria established during run conditions. These experiments show that the approach works for controlling oxygen fugacity in solid media apparatus and can be used to generate fO_2 across nearly 10 orders of magnitude under high pressure conditions not previously accessible for investigation.

Experiments on Mg aluminate spinel demonstrate that V valence is restricted to 3+ over a wide fO_2 and temperature range. Nevertheless, optimized experimental temperature, reducing conditions, and run duration produce spinels with very small V K-edge XANES pre-edges. These measurements are consistent with DFT calculations on spinels of identical chemical composition that point to the stability of V^{3+} at low oxygen fugacities, and the influence of neighboring transition metals in determining the intensity of the V-K pre-edge. The utility of V* valence as an oxybarometer is thus correlated with the site energetics of the spinel rather than with fO_2 directly. fO_2 control of the mineral composition influences the structure and site geometries and thus the intensity of the resulting pre-edge peaks. This additional dependence on composition can thus explain why the correlation of V valence with fO_2 is linear at high oxygen fugacities (>IW-1) and non-linear below those values. Future experiments on aluminous spinels with variable Cr, Ti and Fe^{3+}, might explore how V valence variation depends upon the presence of other cations that may alter the crystal chemical control.

Additional applications of our modified double capsule buffering technique are numerous and might include metal-silicate or mineral-melt element partitioning, phase equilibria studies, or mineral or melt syntheses. However, one must choose buffers carefully and avoid significant reaction between capsules, buffers, and samples for the best application of this approach.

Acknowledgements

This research used resources of the Advanced Light Source and Molecular Foundry, which are DOE Office of Science User Facilities under contract no. DE-AC02-05CH11231. Research funding was provided by an award from the NASA Emerging Worlds program (AJW) and the NASA Planetary Science Division (KR). We thank Sirine Fakra, beamline scientist at

ALS 10.3.2. We thank Roland Montes and Frank Cardenas for machining the Nb, Ta, and Cr buffer capsules, David Shapiro for additional computational support with the Phasis cluster at LBL, and Steve Sutton and an anonymous reviewer for very helpful reviews.

References

Andersson, S. (1967) The Crystal Structure of N−Nb_2O_5, prepared in the presence of small amounts of LiF. Zeitschrift für Anorganische und Allgemeine Chemie, 351, 106-112.

Anisimov, V. I., Aryasetiawan, F. & Lichtenstein, A. I. First-principles calculations of the electronic structure and spectra of strongly correlated systems: the LDA+ U method. *J. Phys.: Condens. Matter* 767–808 (1997).

Arakcheeva, A.V., Grinevich, V.V., Shamrai, V.F., Meyer, M., and Chapuis, G. (1999) KNb_4O_5F and NbO_2 crystal structures. Structural aspect of chemical decomposition of $K_{2-x}Nb_4O_3(O, F)_3F$ in the melt of sodium and potassium chlorides. Crystallography Reports, 44, 2-7.

Armentrout, M.M., Rainey, E.S.G., and Kavner, A. (2013) High pressure and temperature equation of state of cobalt oxide: Implications for redox relations in Earth's mantle. American Mineralogist, 98, 993–999.

Balan, E., De Villiers, J.P., Eeckhout, S.G., Glatzel, P., Toplis, M.J., Fritsch, E., Allard, T., Galoisy, L., and Calas, G. (2006) The oxidation state of vanadium in titanomagnetite from layered basic intrusions. American Mineralogist 91, 953-956.

Ballhaus, C., Berry, R.F., and Green, D.H. (1991) High pressure experimental calibration of the olivine-orthopyroxene-spinel oxygen geobarometer: implications for the oxidation state of the upper mantle. Contributions to Mineralogy and Petrology, 107, 27-40.

770 Barin, I. (1995) Thermochemical Data of Pure Substances, 3rd Ed., Wiley-VCH Verlag GmbH,
771 Germany.
772 Begum, V., Gruner, M.E., Vorwerk, C., Draxl, C., and Pentcheva, R. (2021) Theoretical
773 description of optical and x-ray absorption spectra of MgO including many-body effects.
774 Physical Review B, 103, 195128.
775 Bindeman, I.N., Davis, A.M., and Drake, M.J. (1998) Ion microprobe study of plagioclase-basalt
776 partition experiments at natural concentration levels of trace elements. Geochimica et
777 Cosmochimica Acta, 62, 1175-1193.
778 Bosi, F., Skogby, H., Fregola, R.A., and Hålenius, U. (2016) Crystal chemistry of spinels in the
779 system $MgAl_2O_4$-MgV_2O_4-Mg_2VO_4. American Mineralogist, 101, 580-586.
780 Bowen, N.L. (1915) The crystallization of haplobasaltic, haplodioritic, and related magmas.
781 American Journal of Science, 236, 161-185.
782 Brooker, R., Holloway, J. R., Hervig, R. (1998) Reduction in piston-cylinder experiments: The
783 detection of carbon infiltration into platinum capsules. American Mineralogist, 83, 985-994.
784 Bruschini, E., Speziale, S., Andreozzi, G.B., Bosi, F., and Hålenius, U. (2015) The elasticity of
785 $MgAl_2O_4$–$MnAl_2O_4$ spinels by Brillouin scattering and an empirical approach for bulk
786 modulus prediction. American Mineralogist, 100, 644–651.
787 Cabaret, D., Bordage, A., Juhin, A., and Arfaoui, M. (2010) First-principles calculations of X-ray
788 absorption spectra at the K-edge of 3d transition metals: an electronic structure analysis of
789 the pre-edge. Physical Chemistry Chemical Physics, 12, 5619-5633.
790 Capdevila-Cortada, M., Łodziana, Z., and López, N. (2016) Performance of DFT+ U Approaches
791 in the Study of Catalytic Materials. ACS Catalysis, 6, 8370–8379.

792 Campbell, A.J., Danielson, L., Righter, K., Seagle, C.T., Wang, Y., and Prakapenka, V.B. (2009)
793 High pressure effects on the iron–iron oxide and nickel–nickel oxide oxygen fugacity
794 buffers. Earth and Planetary Science Letters, 286, 556-564.
795 Connolly Jr, H.C., and Burnett, D.S. (2003) On type B CAI formation: experimental constraints
796 on fO_2 variations in spinel minor element partitioning and reequilibration effects.
797 Geochimica et Cosmochimica Acta, 67, 4429-4434.
798 Dal Corso, A. (2014) Pseudopotentials periodic table: From H to Pu. Computational Materials
799 Science, 95, 337-350.
800 Dobson, D.P., and Brodholt, J.P. (1999) The pressure medium as a solid-state oxygen
801 buffer. Geophysical Research Letters, 26, 259-262.
802 Giannozzi, P., Andreussi, O., Brumme, T., Bunau, O., Nardelli, M.B., Calandra, M., Car, R.,
803 Cavazzoni, C., Ceresoli, D., Cococcioni, M., and Colonna, N. (2017) Advanced capabilities
804 for materials modelling with Quantum ESPRESSO. Journal of Physics: Condensed
805 Matter, 29, 465901.
806 Giannozzi, P., Baroni, S., Bonini, N., Calandra, M., Car, R., Cavazzoni, C., Ceresoli, D.,
807 Chiarotti, G.L., Cococcioni, M., Dabo, I., and Dal Corso, A. (2009) QUANTUM
808 ESPRESSO: a modular and open-source software project for quantum simulations of
809 materials. Journal of physics: Condensed matter, 21, 395502.
810 Gougoussis, C., Calandra, M., Seitsonen, A.P., and Mauri, F. (2009) First-principles calculations
811 of x-ray absorption in a scheme based on ultrasoft pseudopotentials: From α-quartz to high-T
812 c compounds. Physical Review B, 80, 075102.

Gougoussis, C., Calandra, M., Seitsonen, A., Brouder, Ch., Shukla, A., and Mauri, F. (2009) Intrinsic charge transfer gap in NiO from Ni K-edge x-ray absorption spectroscopy. Physical Review B, 79, 045118.

Gainsforth, Z. (2020) https://www.github.com/ZGainsforth/QEScripts

Hirel, P. (2015) Atomsk: a tool for manipulating and converting atomic data files. Computer Physics Communications, 197, 212-219.

Horn, I., Foley, S.F., Jackson, S.E., and Jenner, G.A. (1994) Experimentally determined partitioning of high field strength-and selected transition elements between spinel and basaltic melt. Chemical Geology, 117, 193-218.

Huang, H. (2020) http://www.quantumvitas.org

Huebner, J.S. (1971) Buffering techniques for hydrostatic systems at elevated pressures. In (Ulmer, G.C., ed), Research techniques for high pressure and high temperature, p. 123-177, Springer, Berlin, Heidelberg, Germany.

Jacob, K.T., Shekhar, C., Vinay, M., and Waseda, Y. (2010) Thermodynamic properties of niobium oxides. Journal of Chemical & Engineering Data, 55, 4854-4863.

Jilly-Rehak, C.E., Butterworth, A.L., Gainsforth, Z., and Westphal, A.J. (2017) Measuring V-XANES in Aluminum-Rich Chondrules to Probe Oxygen Fugacity Conditions in the Early Solar Disk. 48th Lunar Planetary Science Conference, Lunar and Planetary Institute Contribution No. 1964, abstract #2480.

Keshav, S., Gudfinnsson, G.H., Sen, G. and Fei, Y. (2004) High-pressure melting experiments on garnet clinopyroxenite and the alkalic to tholeiitic transition in ocean-island basalts. Earth and Planetary Science Letters, 223, 365–379.

Klemme, S., and O'Neill, H.S. (1997) The reaction $MgCr_2O_4+SiO_2=Cr_2O_3+MgSiO_3$ and the free energy of formation of magnesiochromite ($MgCr_2O_4$). Contributions to Mineralogy and Petrology, 130, 59-65.

Martin, A.M., and Righter, K. (2013) Melting of clinopyroxene+ magnesite in iron-bearing planetary mantles and implications for the Earth and Mars. Contributions to Mineralogy and Petrology, 166, 1067-1098.

Matjuschkin, V., Brooker, R.A., Tattitch, B., Blundy, J.D. and Stamper, C.C. (2015) Control and monitoring of oxygen fugacity in piston cylinder experiments. Contributions to Mineralogy and Petrology, 169, 9.

McCoy, T.J., Dickinson, T.L., and Lofgren, G.E. (1999) Partial melting of the Indarch (EH4) meteorite: A textural, chemical, and phase relations view of melting and melt migration. Meteoritics & Planetary Science, 34, 735-746.

Medard E., McCammon C.A., Barr J.A., and Grove T.L. (2008) Oxygen fugacity, temperature reproducibility, and H_2O content for nominally dry piston-cylinder experiments using graphite capsules. American Mineralogist, 93, 38–1844.

Morishita, M., Kinoshita, Y., Nozaki, A., Yamamoto, H. (2018) Thermodynamic properties for $MMoO_4$ (M= Mg, Sr and Ba) as the end-members of the yellow phases formed in the nuclear fuel waste glasses. Applied Geochemistry, 98, 310-320.

O'Neill, H.S.C., and Pownceby, M.I. (1993) Thermodynamic data from redox reactions at high temperatures. I. An experimental and theoretical assessment of the electrochemical method using stabilized zirconia electrolytes, with revised values for the Fe-"FeO", Co-CoO, Ni-NiO and Cu-Cu_2O oxygen buffers, and new data for the W-WO_2 buffer. Contributions to Mineralogy and Petrology, 114, 296-314.

Okamato, H., Binary Alloy Phase Diagrams. 2nd ed. 1990: ASM International.Otero-de-la-Roza, A., Johnson, E. R., and Luaña, V. (2014) Critic2: A program for real-space analysis of quantum chemical interactions in solids. Computational Physics Communications 185, 1007-1018.

Palmer, D.C. (2015) Visualization and analysis of crystal structures using CrystalMaker software. Zeitschrift für Kristallographie-Crystalline Materials, 230, 559-572.

Pawley, A.R., Holloway, J.R., and McMillan, P.F. (1992) The effect of oxygen fugacity on the solubility of carbon-oxygen fluids in basaltic melt. Earth and Planetary Science Letters, 110, 213-225.

Paque, J.M., Sutton, S.R., Simon, S.B., Beckett, J.R., Burnett, D.S., Grossman, L., Yurimoto, H., Itoh, S., and Connolly Jr, H.C. (2013) XANES and Mg isotopic analyses of spinels in Ca-Al-rich inclusions: Evidence for formation under oxidizing conditions. Meteoritics & Planetary Science, 48, 2015-2043.

Pearce, C. I. Henderson, C.M.B., Telling, N.D., Pattrick, R.A., Charnock, J.M., Coker, V.S., Arenholz, E., Tuna, F., and van der Laan, G. (2010) Fe site occupancy in magnetite-ulvospinel solid solutions: A new approach using X-ray magnetic circular dichroism. American Mineralogist, 95, 425–439.

Perdew, J.P., Burke, K., and Ernzerhof, M. (1996) Generalized Gradient Approximation Made Simple. Physical Review Letters, 77, 3865–3868.

Pownceby, M. I., and O'Neill, H.S.C. (1994) Thermodynamic data from redox reactions at high temperatures. IV. Calibration of the Re-ReO_2 oxygen buffer from EMF and NiO+ Ni-Pd redox sensor measurements. Contributions to Mineralogy and Petrology, 118, 130-137.

880 Prendergast, D., and Galli, G. (2006) X-Ray Absorption Spectra of Water from First Principles
881 Calculations. Physical Review Letters, 96, 215502.
882 Raghavan, S. (1991) Gibbs energy of formation of mon-magnesium niobate using a solid state
883 galvanic cell. Transactions of the Indian Institute of Metallurgy, 44, 39-44.
884 Raghavan, S., and Kay, D.A.R. (1990) Gibbs free energy of formation of magnesium tungstate
885 from emf measurements. Thermochimica Acta, 170, 13-17.
886 Righter, K., and Hauri, E.H. (1998) Compatibility of rhenium in garnet during mantle melting
887 and magma genesis. Science, 280, 1737-1741.
888 Righter, K., Sutton, S.R., Danielson, L., Pando, K., and Newville, M. (2016) Redox variations in
889 the inner solar system with new constraints from vanadium XANES in spinels. American
890 Mineralogist, 101, 1928-1942.
891 Righter, K., Pando, K.M., Danielson, L., and Lee, C.T. (2010) Partitioning of Mo, P and other
892 siderophile elements (Cu, Ga, Sn, Ni, Co, Cr, Mn, V, and W) between metal and silicate melt
893 as a function of temperature and silicate melt composition. Earth and Planetary Science
894 Letters, 291, 1-9.
895 Righter, K., Sutton, S.R., Newville, M., Le, L., Schwandt, C.S., Uchida, H., ... and Downs, R.T.
896 (2006) An experimental study of the oxidation state of vanadium in spinel and basaltic melt
897 with implications for the origin of planetary basalt. American Mineralogist, 91, 1643-1656.
898 Robie, R.A., Hemingway, R.S., and Fisher, J.R. (1978) Thermodynamic properties of minerals
899 and related substances at 298.15 K and 1 bar (10^5 pascals) pressure and at higher
900 temperatures. United States Geological Survey Bulletin 1452. United States Government
901 Printing Office, Washington.

902 Roeder, P.L., and Reynolds, I. (1991) Crystallization of chromite and chromium solubility in
903 basaltic melts. Journal of Petrology, 32, 909-934.
904 Rubie, D.C. (1999) Characterising the sample environment in multi anvil high-pressure
905 experiments. Phase Transitions, 68, 431-451.
906 Sheng, Y.J., Wasserburg, G.J., and Hutcheon, I. D. (1992) Self-diffusion of magnesium in spinel
907 and in equilibrium melts: Constraints on flash heating of silicates. Geochimica et
908 Cosmochimica Acta, 56, 2535-2546.
909 Shofner, G.A., Campbell, A.J., Danielson, L.R., Righter, K., Fischer, R.A., Wang, Y., and
910 Prakapenka, V. (2016) The W-WO_2 oxygen fugacity buffer (WWO) at high pressure and
911 temperature: Implications for fO_2 buffering and metal-silicate partitioning. American
912 Mineralogist, 101, 211-221.
913 Sievwright, R.H., O'Neill, H.S.C., Tolley, J., Wilkinson, J.J., and Berry, A.J. (2020) Diffusion
914 and partition coefficients of minor and trace elements in magnetite as a function of oxygen
915 fugacity at 1150 ºC. Contributions to Mineralogy and Petrology, 175, 1-21.
916 Sumin, V.V. (1989) Study of NbO compounds by the methods of neutron diffraction and
917 inelastic neutron scattering. Kristallografiya, 34, 655-657.
918 Sutton, S.R., Karner, J., Papike, J.J., Delaney, J.S., Shearer, C., Newville, M., ... and Dyar, M.D.
919 (2005) Vanadium K edge XANES of synthetic and natural basaltic glasses and application to
920 microscale oxygen barometry. Geochimica et Cosmochimica Acta, 69, 2333-2348.
921 Suzuki, A.M., Yasuda, A., and Ozawa, K. (2008) Cr and Al diffusion in chromite spinel:
922 experimental determination and its implication for diffusion creep. Physics and Chemistry of
923 Minerals, 35, 433-445.

924 Taillefumier, M., Cabaret, D., Flank, A.M., and Mauri, F. (2002) X-ray absorption near-edge
925 structure calculations with the pseudopotentials: Application to the K edge in diamond and
926 alpha-quartz, Physical Review B, 66, 195107.
927 Toplis, M.J., and Corgne, A. (2002) An experimental study of element partitioning between
928 magnetite, clinopyroxene and iron-bearing silicate liquids with particular emphasis on
929 vanadium. Contributions to Mineralogy and Petrology, 144, 22-37.
930 Wang, L., Maxisch, T., and Ceder, G. (2006) Oxidation energies of transition metal oxides
931 within the GGA+U framework. Physical Review B, 73, 195107.
932 Wojdyr, M. (2010) Fityk: a general-purpose peak fitting program. Journal of Applied
933 Crystallography, 43, 1126–1128.
934 Yu, M., and Trinkle, D. (2011) Accurate and efficient algorithm for Bader charge integration.
935 Journal of Chemical Physics, 134, 064111.
936
937
938
939
940

941 **Table 1:** Summary of run conditions for the oxygen fugacity calibration experiments (1400 °C, 1 GPa, 3 hrs)
942

Date	expt #	Run #	inner	outer	Buffer	$\log fO_2$ buffer	ΔIW buffer	$\log fO_2$ secondary
8/14/2018	2018 4d	1364	Al_2O_3	Mo	Ta-Ta_2O_5	-16.7	-6.3	-
7/25/2018	2018 2b	1359	Al_2O_3	Mo	Nb-NbO	-16.9	-6.5	-15.0
7/26/2018	2018 3e	1361	Al_2O_3	Mo	Cr-Cr_2O_3	-14.8	-4.4	-15.4
8/13/2018	2018 1b	1363	MgO	Mo	Mo-MoO_2	-9.2	+1.2	-8.9
9/11/2018	2018-6	1376	MgO	Co	Co-CoO	-7.3	+3.1	-8.7
9/13/2018	2018 5d	1377	MgO	W	W-WO_3	-8.8	+1.5	-10.7
4/3/2019	CMAS-7 (2019 1)	1419	Al_2O_3	Co	Co-CoO	-7.3	+3.1	-8.7
4/19/2019	CMAS-9 (2019 2)	1424	Al_2O_3	Ni	Ni-NiO	-5.7	+4.7	-7.3

943

This is the peer-reviewed, final accepted version for American Mineralogist, published by the Mineralogical Society of America.
The published version is subject to change. Cite as Authors (Year) Title. American Mineralogist, in press.
DOI: https://doi.org/10.2138/am-2022-8301. http://www.minsocam.org/

Table 2: Summary of run conditions and EMPA and XANES results for the spinel+1% V_2O_3 series in MgO capsules (all at 1 GPa)

Date	expt #	run #	T	time	outer	buffer	Buffer logfO_2	ΔIW	V XANES pre-edge peak	MgO	NbO	Al_2O_3	V_2O_3	Total	n
Reduced spinels series															
5/9/18	spnl-Ta	1329 ¥	1600	2	Mo	Ta	-13.96	-5.37	26(4)	25.7(5)	-	73.2(1.5)	1.09(2)	100.0	-
4/15/18	spnl-Cr	1324	1600	2.3	Mo	Cr	-12.09	-3.51	26(4)	25.7(5)	-	72.4(1.5)	1.86(4)	100.0	-
1/14/20	Spinel-V-007	E-116	1600	6	Mo	Nb	-14.02	-5.44	14(1)	28.9(6)	0.035(1)	71.5(1.4)	0.277(6)	100.73	25
Time series															
1/7/20	Spinel-V-005	E-114	1600	0.75	Mo	Nb	-14.02	-5.44	20(3)	28.7(6)	0.016(1)	72.2(1.4)	0.117(2)	100.96	23
6/11/19	Spinel-V-001 #2	1430	1600	2.5-3	Mo	Nb	-14.02	-5.44	13(5)	26.4(5)	n.d.	73.6(1.5)	0.131(3)	100.18	24
1/14/20	Spinel-V-007	E-116	1600	6	Mo	Nb	-14.02	-5.44	14(1)	28.9(6)	0.035(1)	71.5(1.4)	0.277(6)	100.73	25
2/19/20	Spinel-V-009	E-120	1600	24	Mo	Nb	-14.02	-5.44	-	28.9(6)	0.385(8)	71.0(1.4)	0.099(2)	100.32	27
1/21/20	Spinel-V-008	E-117	1600	70	Mo	Nb	-14.02	-5.44	18(6)	28.7(6)	0.23(1)	70.9(1.4)	0.103(2)	99.87	20

¥ 0.5 GPa, and 2% V_2O_3 added to spinel

Most analyses were done by electron microprobe; spnl-Ta and spnl-Cr were done using the Tescan SEM.

This is the peer-reviewed, final accepted version for American Mineralogist, published by the Mineralogical Society of America.
The published version is subject to change. Cite as Authors (Year) Title. American Mineralogist, in press.
DOI: https://doi.org/10.2138/am-2022-8301. http://www.minsocam.org/

951 **Figure Captions**

952 **Figure 1A:** Calculations of fO_2 for each of the buffers used, relative to the iron-wüstite buffer
953 (ΔIW). At the temperature of our experiments (1400 °C), the range of fO_2 covered is from
954 IW+4.5 to IW-6.5; the temperature dependence of most buffers is weak. Thermodynamic data
955 mainly from Barin et al. (1995), with additional data from Raghavan and Kay (1990)
956 (magnesium tungstate) and Pownceby and O'Neill (1994) (Re-ReO_2) (see **Table S4** for more
957 details and additional buffers not shown here for clarity). Note that the Ta-Ta_2O_5 (long dash)
958 and V-V_2O_3 (solid) buffer curves are very similar and overlap across nearly the entire range
959 shown. **Figure 1B:** Comparison of relative fO_2 (ΔIW) achievable by gas mixing, compared to
960 that defined by various metal-oxide buffers. The values shown for the buffers are calculated for
961 1 bar and 1400 °C; values of the buffers at 1 GPa will be shifted to slightly higher values than 1
962 bar due to the volume change which typically corresponds to ~0.15 to 0.4 log(fO_2) units
963 depending on the specific metal-oxide pair.

964 **Figure 2A:** Schematic illustration of the modified double capsule technique used in this study.
965 **Figure 2B**: Schematic illustration of one variation which employed a molybdenum (Mo) outer
966 capsule that enclosed the buffer metal and oxide as well as the inner capsule**. Figure 2C**:
967 Schematic illustration of a second variation which employed a disk or foil plate of metal buffer
968 (Ni or Co) between the oxide buffer (NiO or CoO) and the inner capsule to prevent reaction and
969 dissolution of the buffer oxide into the inner ceramic capsule. **Figure 2D:** a false color BSE
970 image of experiment at 1400 °C, showing the outer capsule (Mo) enclosing the Nb and NbO
971 buffer, the inner capsule (MgO), and spinel sample in a real experiment. This modified double
972 capsule approach is the variation portrayed in Figure 2B.

973 **Figure 3:** The 2x2x2 superlattice cell of Fe-Cr bearing spinel with an octahedral V in the center.
974 Polyhedra of several neighboring atoms are also highlighted. This spinel corresponds to
975 "Magnesiochromite" in **Table S3** and was formed one log fO_2 unit below the IW buffer (IW-1).
976 The local geometry around the V atom is not perfectly symmetric because the neighboring atoms
977 are not symmetrically positioned. The grey V atom in the middle of the cell is obscured by the
978 light blue Al atom. The red, green, and blue axes are the unit cell x,y,z axes. CrystalMaker was
979 used to construct this diagram: http://www.crystalmaker.com.

980 **Figure 4A-J:** BSE images of buffers and glasses produced in the series of CMAS glass
981 experiments, from top to bottom: Ta (Figure 4A,B), Nb (Figure 4C,D), Cr (Figure 4E,F), Mo
982 (Figure 4G,H), and W (Figure 4I,J) buffers. For each experiment is shown an image of the
983 buffer assembly (left) and the CMAS glass run product (right). The Ta, Nb, and W buffered
984 experiments were carried out with a Mo outer capsule (Fig. 4A, 4C, and 4I, respectively) that
985 helped to maintain the buffer assemblage for longer durations (see text for discussion). The Cr,
986 Mo and W experiments also produced a reaction product between MgO capsule and buffer
987 materials – $MgCr_2O_4$, $MgMoO_4$, and $MgWO_4$, (Fig. 4E, 4G, and 4I, respectively; see text for
988 discussion). Some of the CMAS glasses also contain plagioclase feldspar that is expected to be
989 stable in the melt composition and PT range (darker phase within the glass in Figures 4B, 4F,
990 and 4J). The presence of plagioclase does not affect the results of our series and the glasses
991 produced in all experiments are within the range of compositions for CMAS systems glasses
992 used by Sutton et al. (2005). All scale bars 10 μm.

993 **Figure 5A:** BSE image of experiment 1359 (2018 2b) carried out for the CMAS glass series
994 using Nb-Nb oxide buffer. The image shows bright Nb metal, intermediate gray Nb oxide, and

995 darkest phase is the alumina capsule. **Figure 5B:** an EBSD map showing the two structurally
996 distinct Nb oxides - NbO and NbO_2 intergrown with one another.

997 **Figure 6A:** Stacked V XANES spectra for CMAS glasses equilibrated using outer capsule
998 buffers Mo-MoO_2, W-WO_3, Ni-NiO, Co-CoO, Ta-Ta_2O_5, Cr-Cr_2O_3, and Nb-Nb_2O_5. **Figure 6B:**
999 Superimposed pre-edges for the V XANES for comparison.

1000 **Figure 7A-F:** Spinel-V_2O_3 textures in reduced spinel experiments at 1600 °C, including
1001 experiments 1329 with the Ta-Ta_2O_5 buffer (A,B), 1324 with the Cr-Cr_2O_3 buffer (C,D) and E-
1002 116 (V-008) with the Nb-NbO buffer (E,F). Left hand images (A, C, and E) show the buffer
1003 materials, and the right hand images (B, D, and F) show the spinel sample textures.

1004 **Figure 8A:** Spinel V-K XANES spectra from the Nb-NbO buffered experimental $MgAl_2O_4$
1005 spinel (V-008), magnesiochromite (IW-1 from Righter et al., 2006), and magnetite-
1006 magnesioferrite (run 202 from Righter et al., 2006). **Figure 8B:** V-K XANES pre-edge peaks
1007 from spinel spectra in Figure 8A.

1008 **Figure 9A:** V-K XANES of magnesiospinel ($MgAl_2O_4$), experimental vs theoretical. **Figure**
1009 **9B:** Pre-edges for spinels of various composition predicted by DFT and DFT+U. **Figure 9C:**
1010 Comparison of theoretical pre-edge intensities calculated by DFT (round dots with color) and
1011 experimental values measured by synchrotron (black shapes). By including the correct physical
1012 phenomena, the $MgAl_2O_4$ and Fe_3O_4-rich spinels were correctly simulated. The intermediate
1013 magnesiochromite was not faithfully simulated (see text).

1014 **Figure 10:** Comparison of log(fO_2) expected from the buffer and log(fO_2) calculated based on
1015 the secondary equilibrium characterized in each experiment. Solid line is a fit to the data with an
1016 R^2 of 0.933. LogfO_2 for the various metal-oxide buffers was calculated using thermodynamic
1017 data from Barin (1995) (see also **Table S4**). The Cr, Ni, and Co equilibria utilized

1018 thermodynamic data from Robie et al. (1978), Nb equilibrium utilized thermodynamic data from
1019 Jacob et al. (2010), W equilibrium utilized thermodynamic data from Raghavan and Kay (1990),
1020 and Mo equilibrium utilized thermodynamic data from Morishita et al. (2018) (see text for
1021 discussion of details of equilibria).

1022 **Figure 11A,B:** Electronic orbitals contributing to the V-K pre-edge in $MgAl_2O_4$ and their
1023 proximity to the Fermi level. **Figure 11A:** The two V-d orbitals above the Fermi level in
1024 $MgAl_2O_4$ with one V atom. They are located more than 2 eV above the Fermi level and
1025 therefore should be able to accept transitions. **Figure 11B:** The two comparable orbitals above
1026 the Fermi level when two Ti atoms are added to the unit cell located 5.0 and 8.7 Å from the V.
1027 The orbitals sit right at the Fermi level and have lower amplitude near the V atom and are not
1028 able to receive transitions. V, Ti atoms are plotted as 1.25 Å diameter spheres, and the O atoms
1029 are plotted as 0.5 Å spheres. The isosurface is plotted in both cases as 1% of the maximum
1030 charge density. B shows that these pre-edge orbitals hybridize significantly with neighboring Ti
1031 atoms thereby reducing the overlap with the V 1s core orbital, due to norm-conservation, and
1032 moving them closer to the Fermi level, which in turn reduces the quadrupole pre-edge intensity.

1033 **Figure 12A:** The relationship between oxygen fugacity of spinel formation and the intensity of
1034 the pre-edge for all spinels measured in this work and in Righter et al. (2006). **Figure 12B**:
1035 comparison of experimental $\log(fO_2)$ and $\log(fO_2)$ calculated using the expression derived here
1036 based on the pre-edge peak intensity (I_{pre}), the pre-edge peak position in eV (E_{pre}) and the atom%
1037 of Mg and O (see text for discussion). Light blue symbols include spinels from Righter et al.
1038 (2006), and from this study. The experimental points are distributed around the line horizontally
1039 by a standard deviation of 1.2 log units; regression has an R^2 of 0.87.

1040

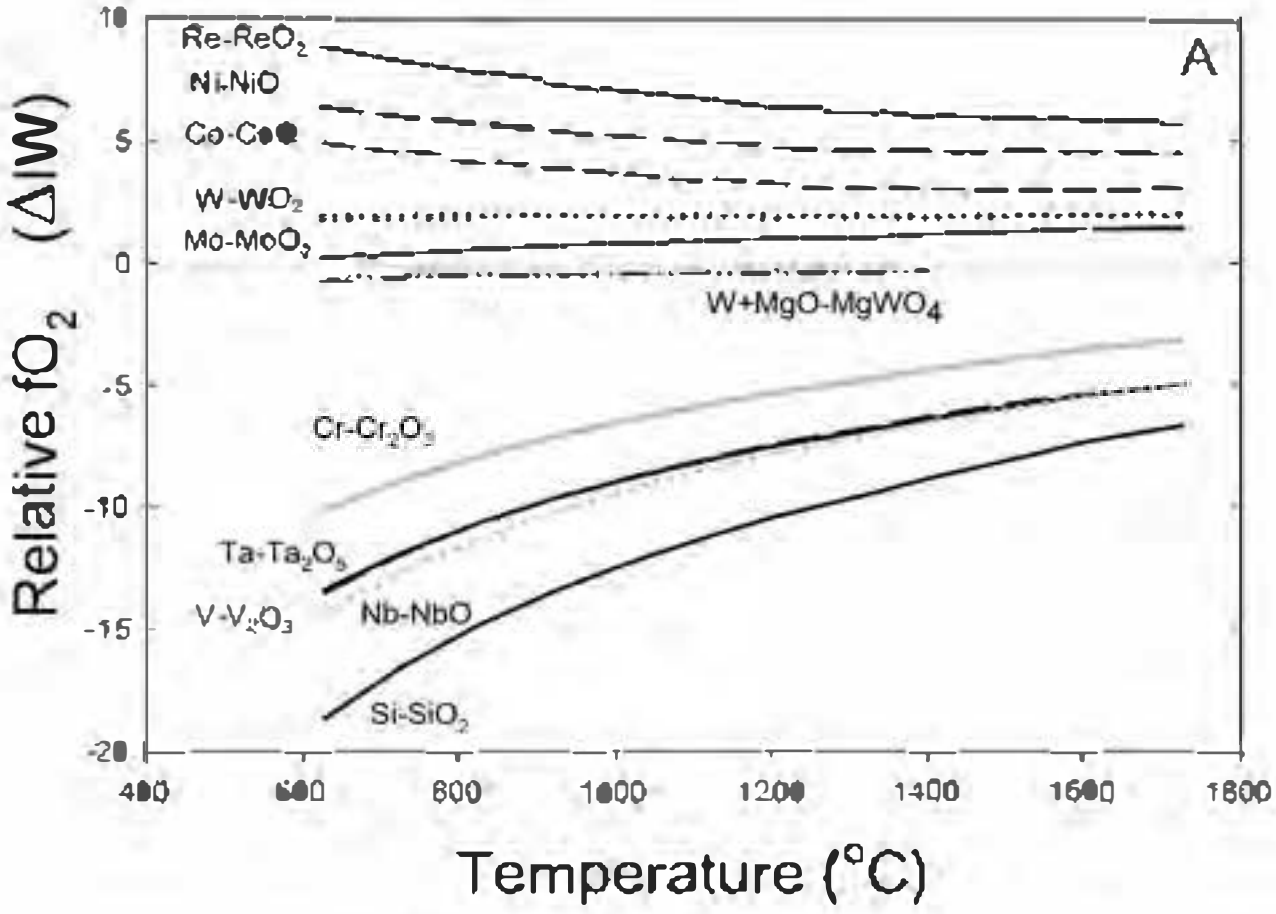

Oxygen fugacity in experimental systems and natural materials

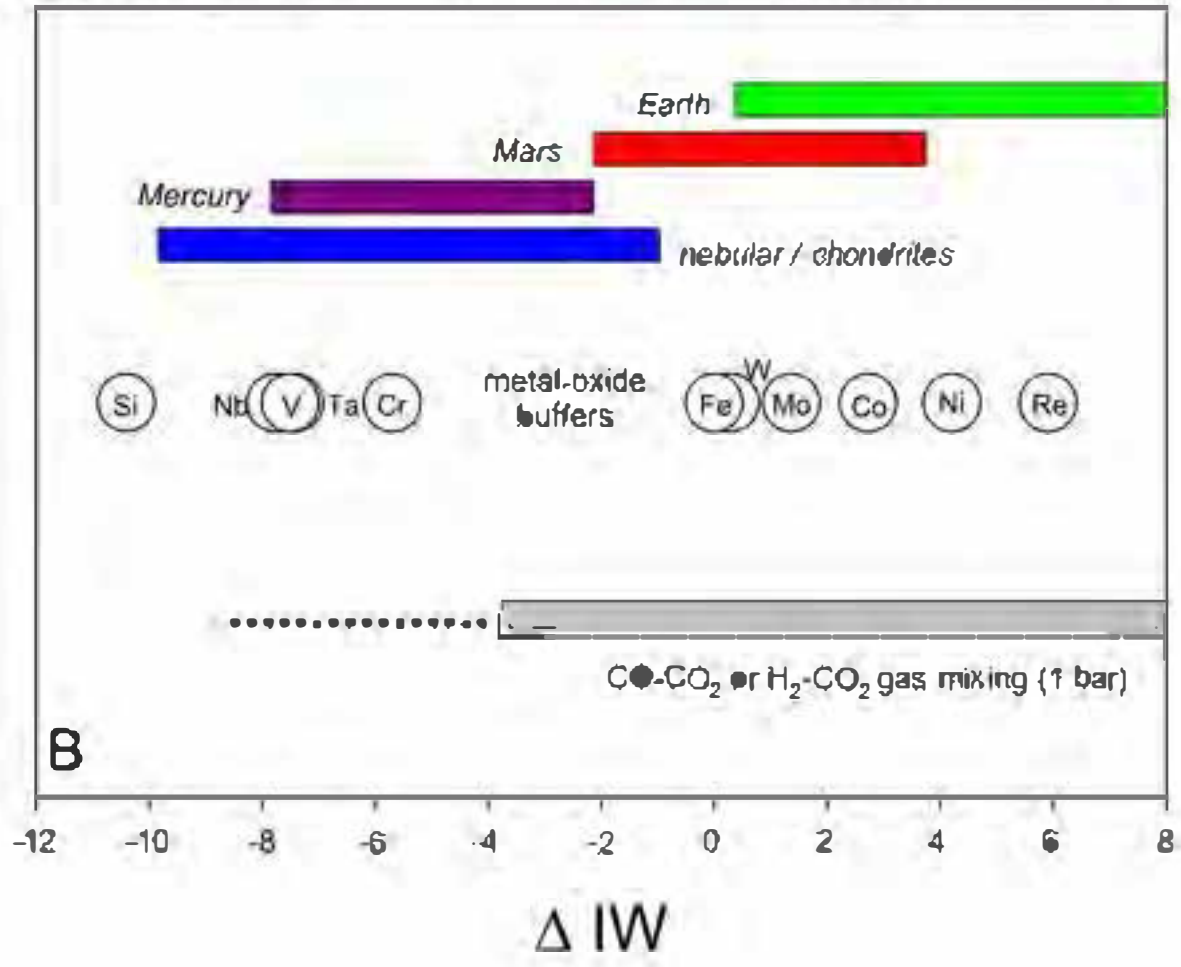

Figure 1

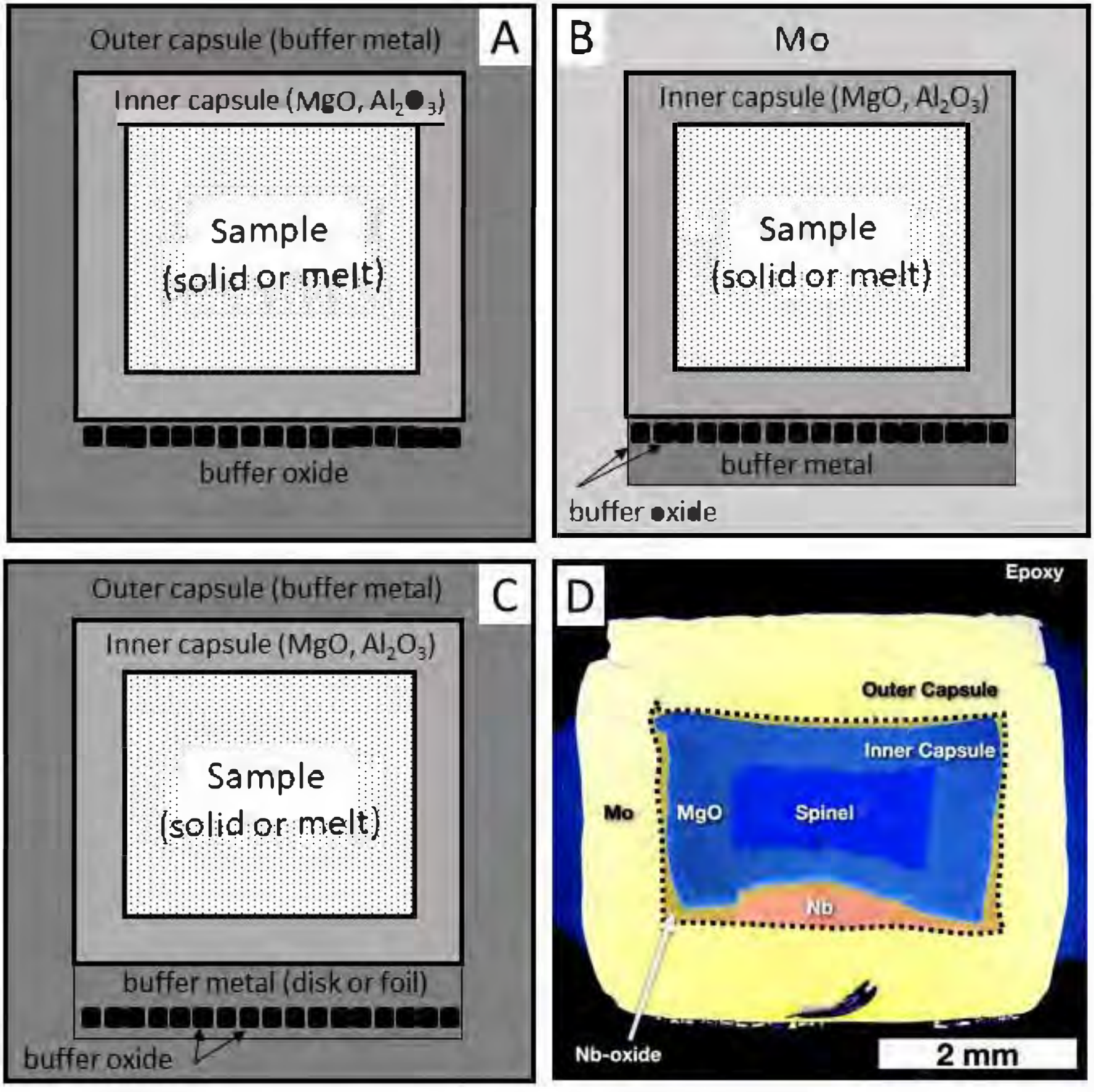
A
Outer capsule (buffer metal)
Inner capsule (MgO, Al_2O_3)
Sample
(solid or melt)
buffer oxide
B
Mo
Inner capsule (MgO, Al_2O_3)
Sample
(solid or melt)
buffer metal
buffer oxide
C
Outer capsule (buffer metal)
Inner capsule (MgO, Al_2O_3)
Sample
(solid or melt)
buffer metal (disk or foil)
buffer oxide
D
Epoxy
Outer Capsule
Inner Capsule
Mo
MgO
Spinel
Nb
Nb-oxide
2 mm

Figure 2

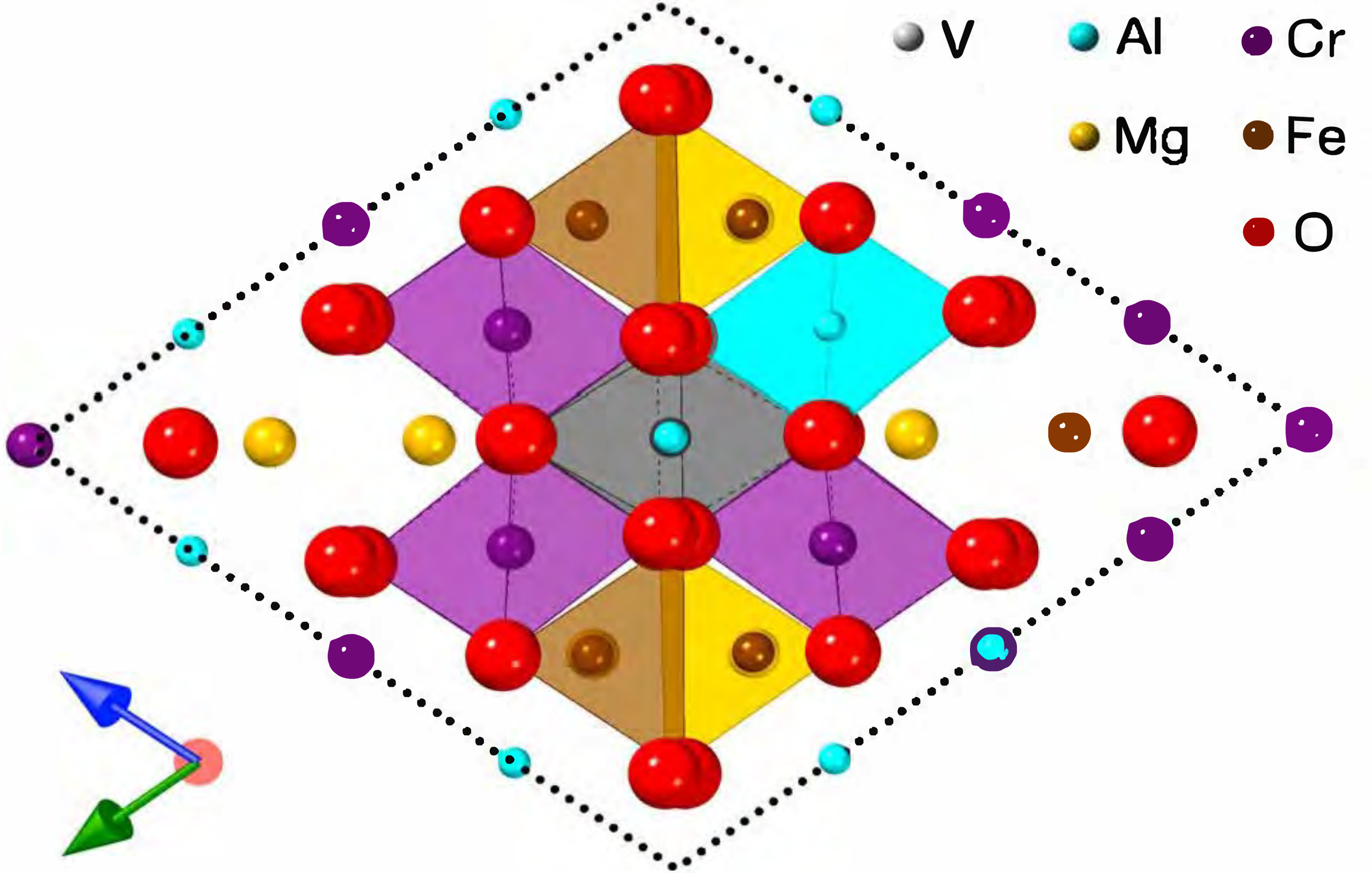

Figure 3

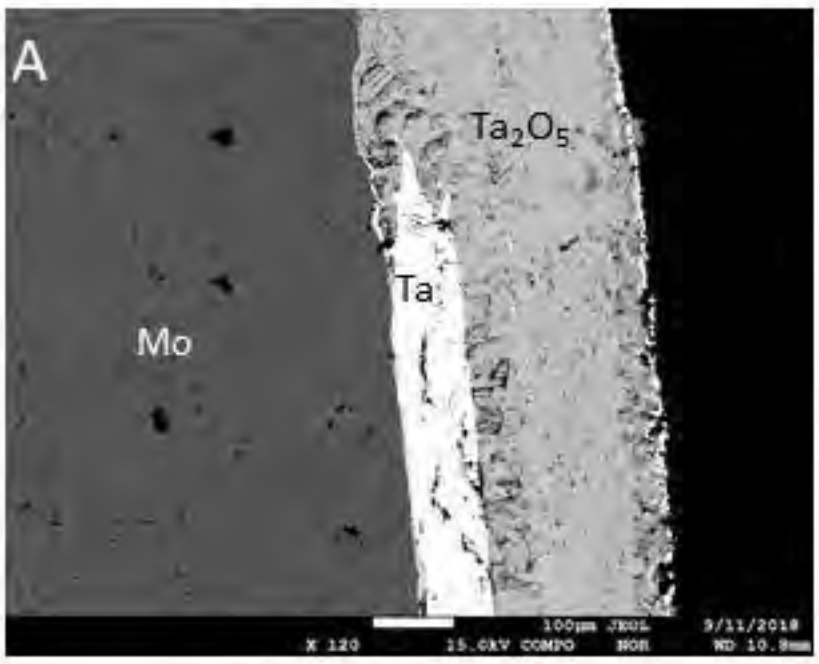
A
Ta_2O_5
Ta
Mo

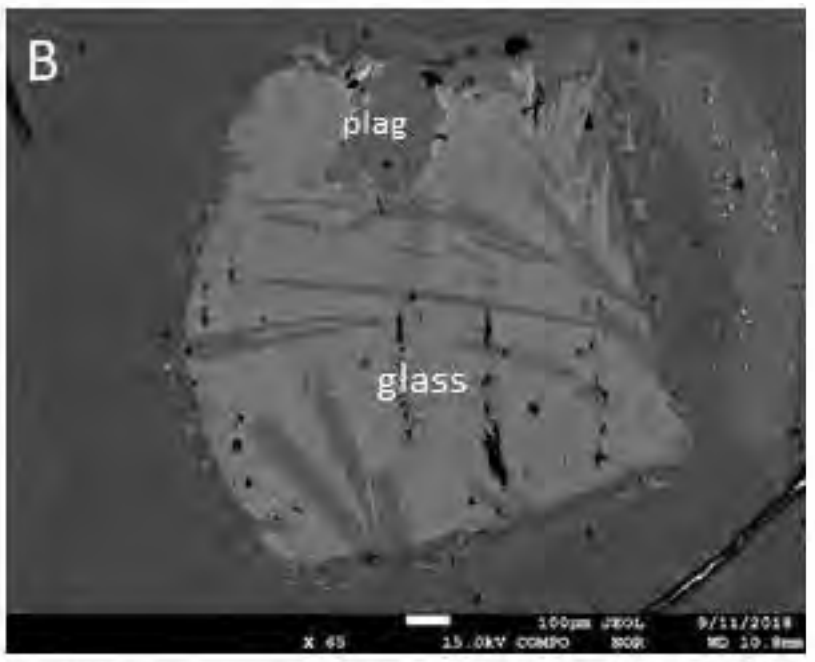
B
plag
glass

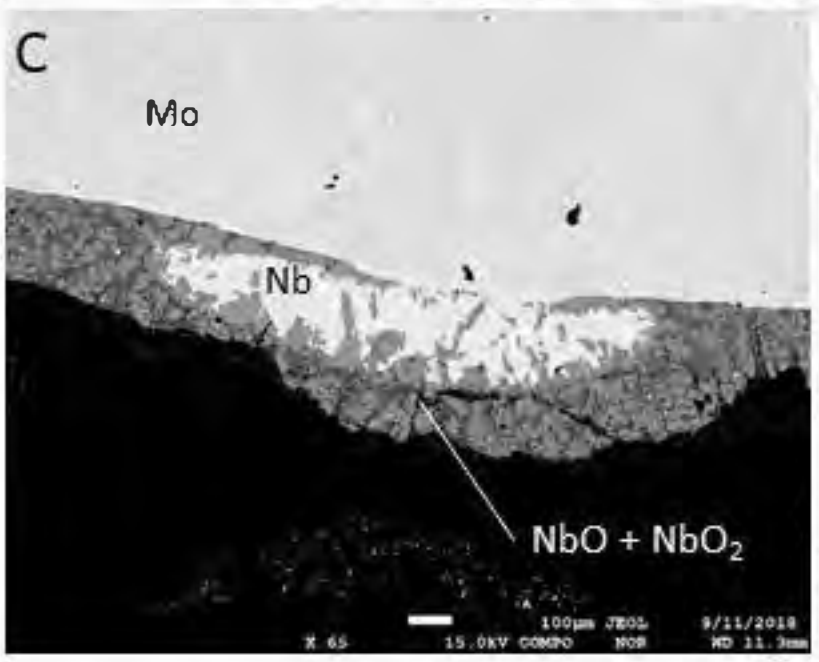
C
Mo
Nb
$NbO + NbO_2$

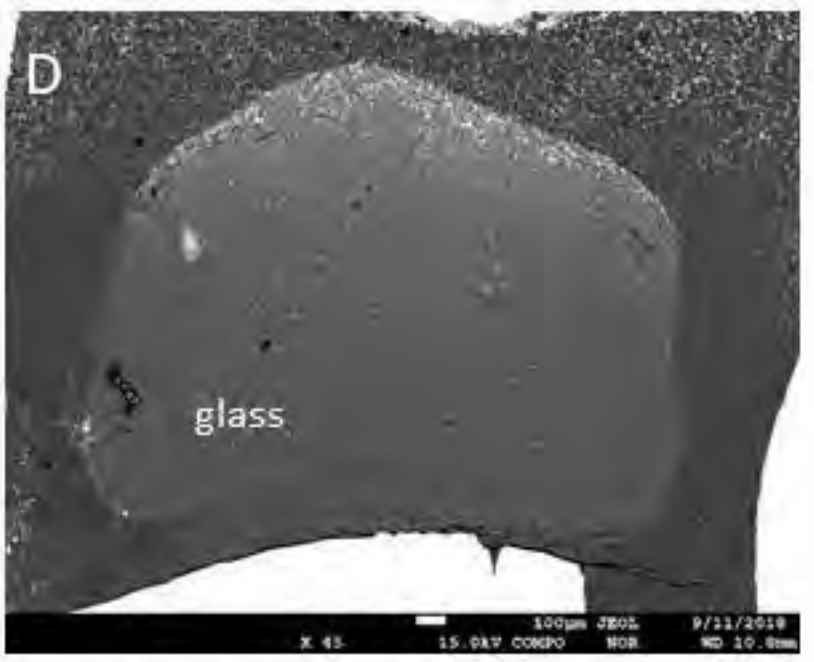
D
glass

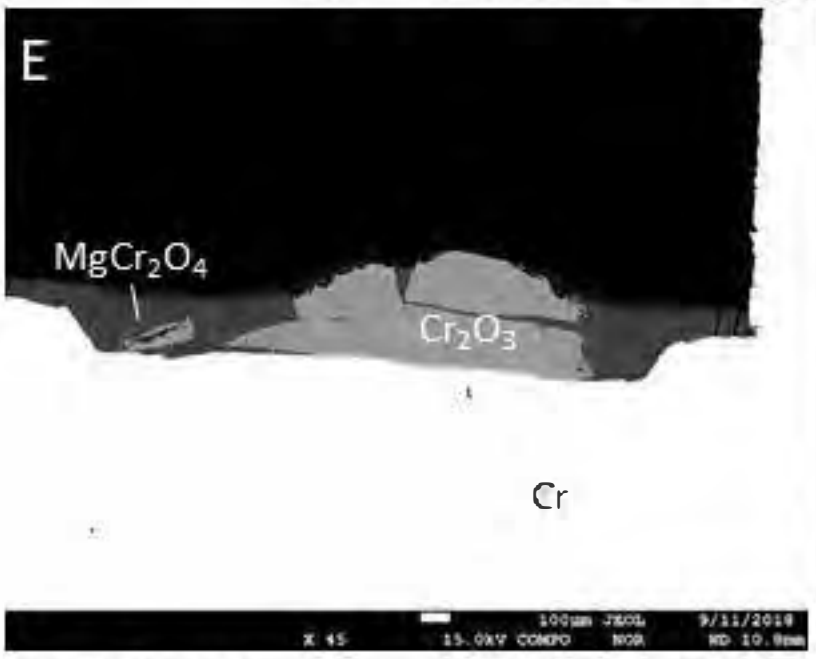
E
$MgCr_2O_4$
Cr_2O_3
Cr

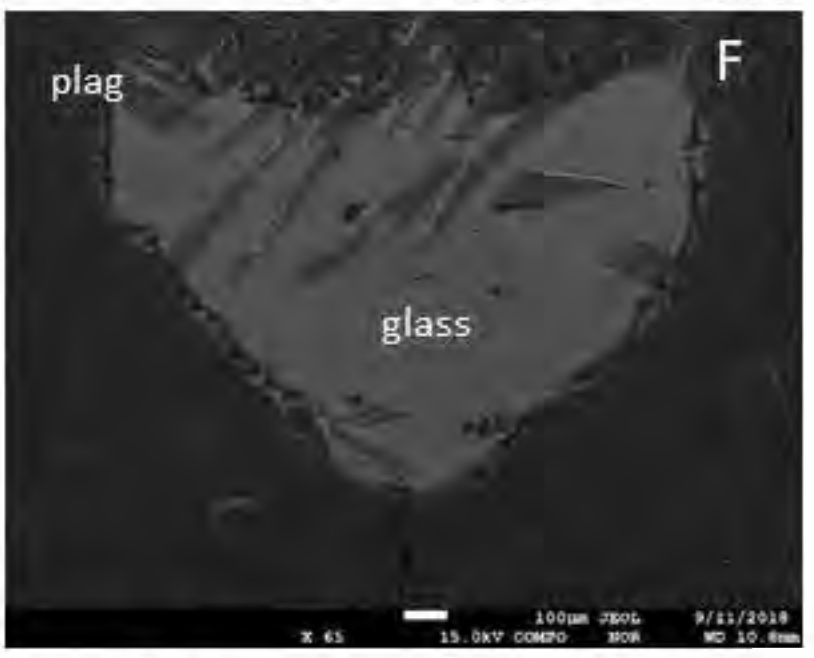
plag
F
glass

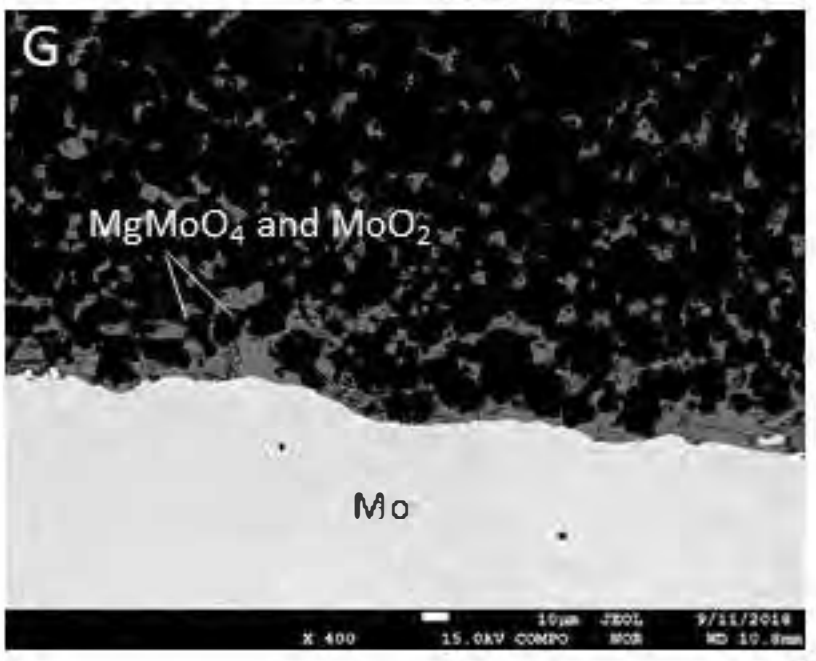
G
$MgMoO_4$ and MoO_2
Mo

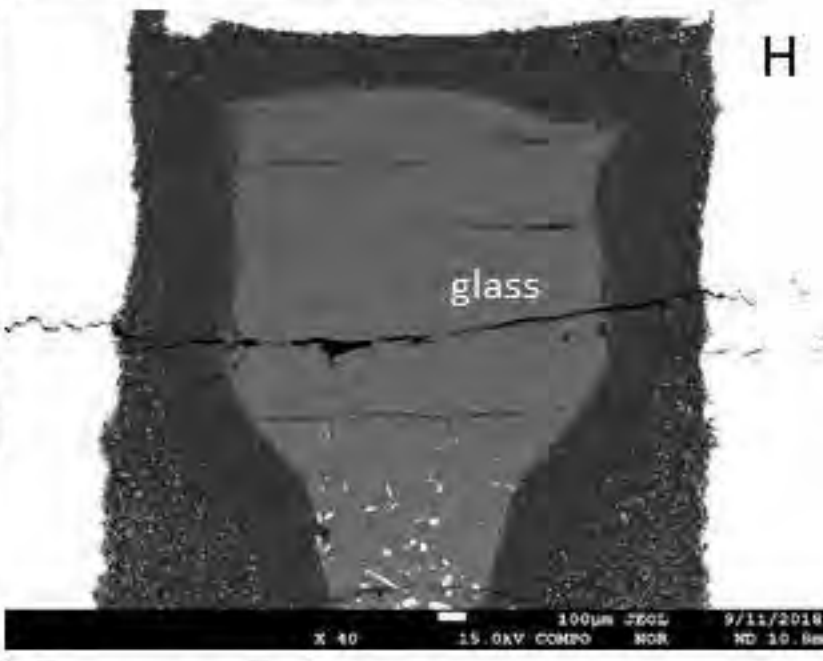
H
glass

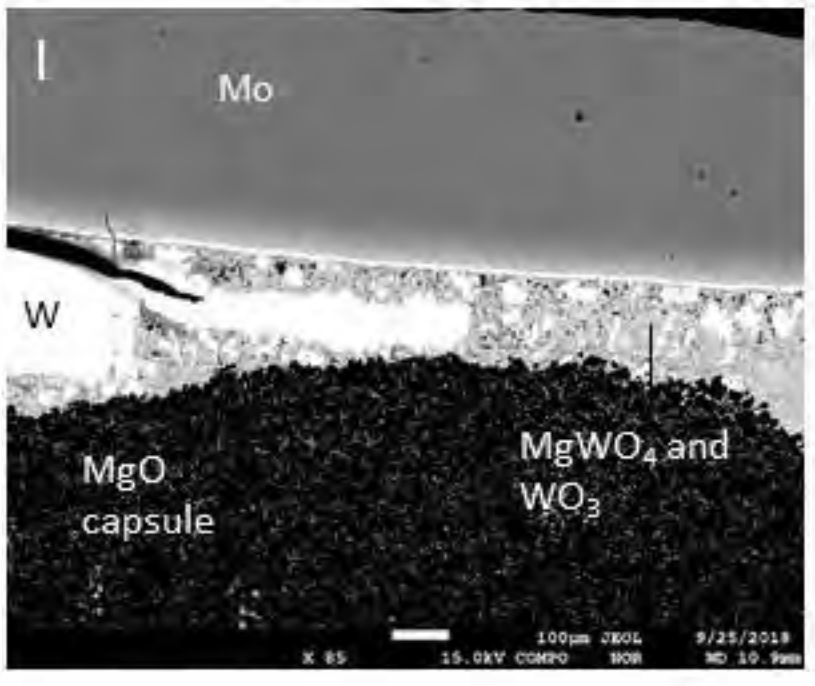
I
Mo
W
MgO
capsule
$MgWO_4$ and
WO_3


MgO
capsule
J
glass + plag

Figure 4

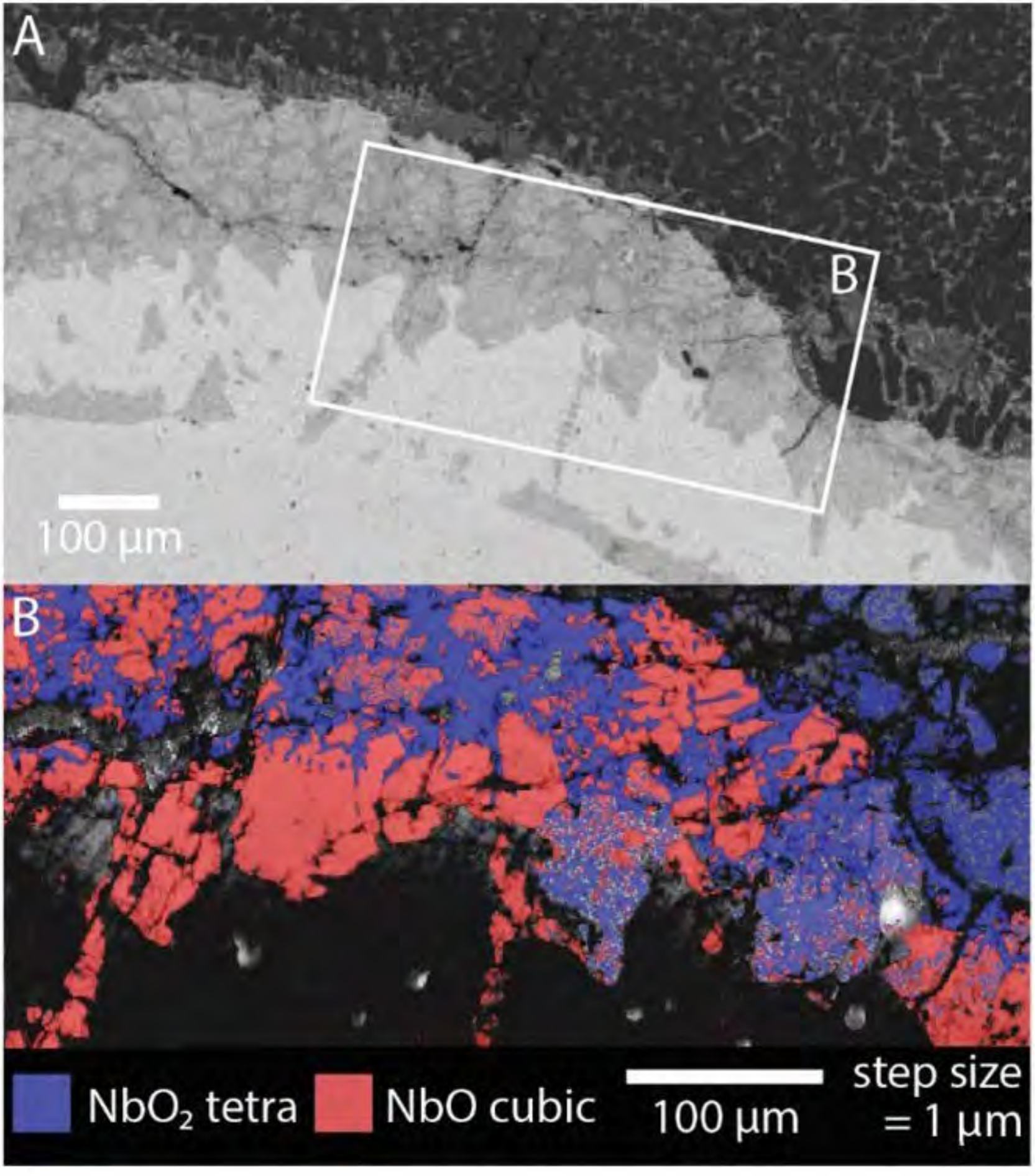

Figure 5

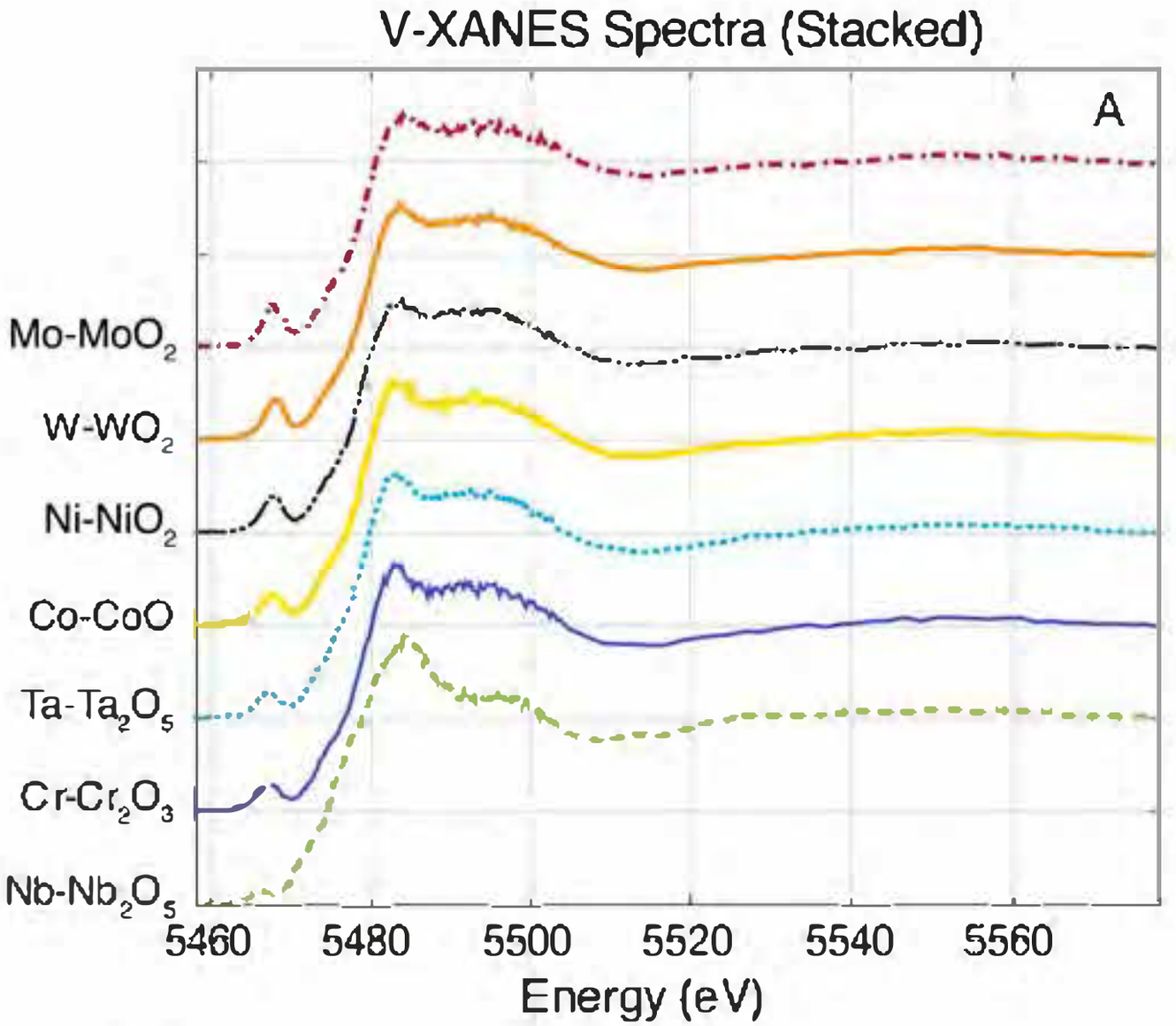
V-XANES Spectra (Stacked)
A
Mo-MoO2
W-WO2
Ni-NiO2
Co-CoO
Ta-Ta2O5
Cr-Cr2O3
Nb-Nb2O5
5460
5480
5500
5520
5540
5560
Energy (eV)

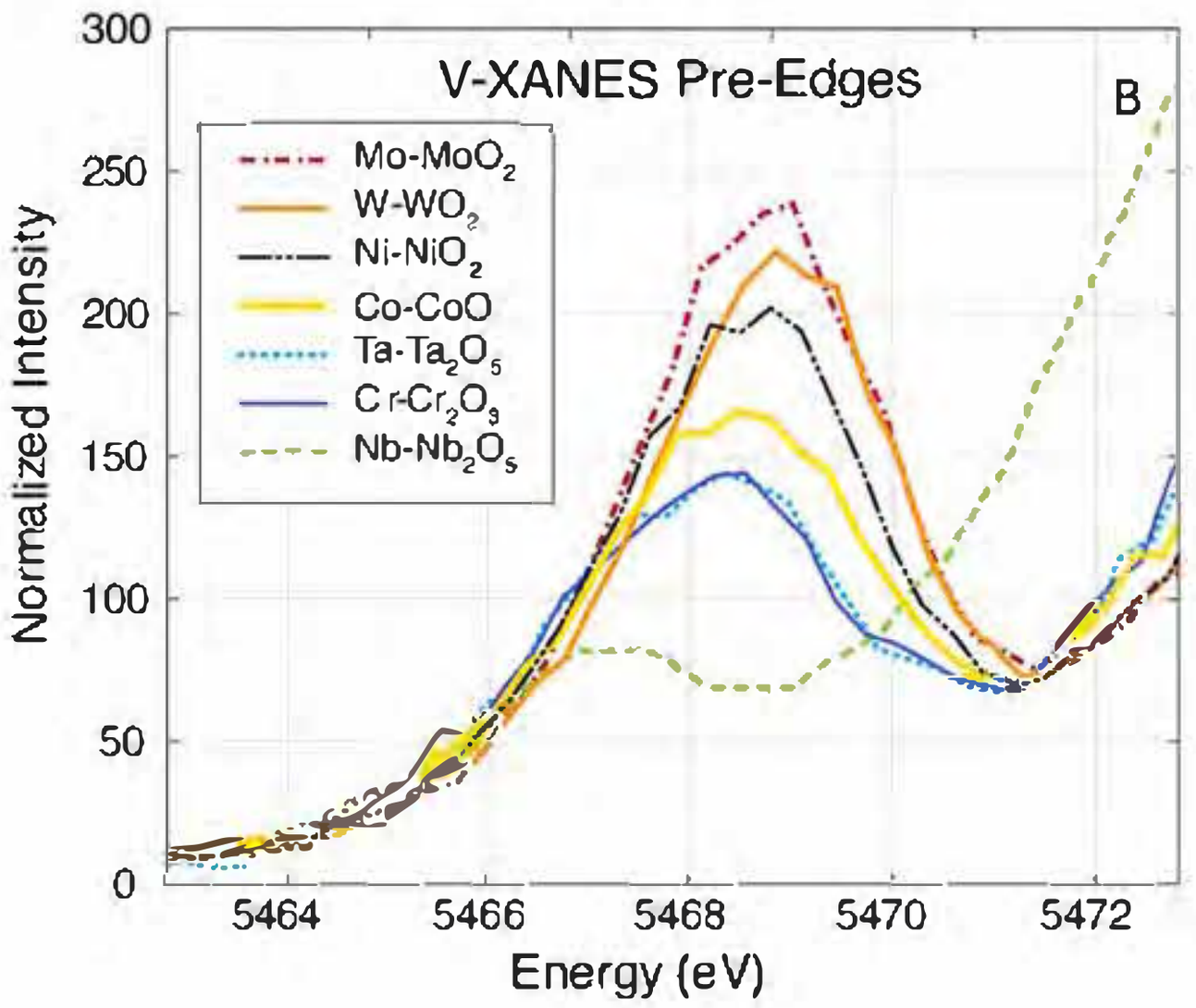
V-XANES Pre-Edges
B
Mo-MoO2
W-WO2
Ni-NiO2
Co-CoO
Ta-Ta2O5
Cr-Cr2O3
Nb-Nb2O5
Normalized Intensity
300
250
200
150
100
50
0
5464
5466
5468
5470
5472
Energy (eV)

Figure 6

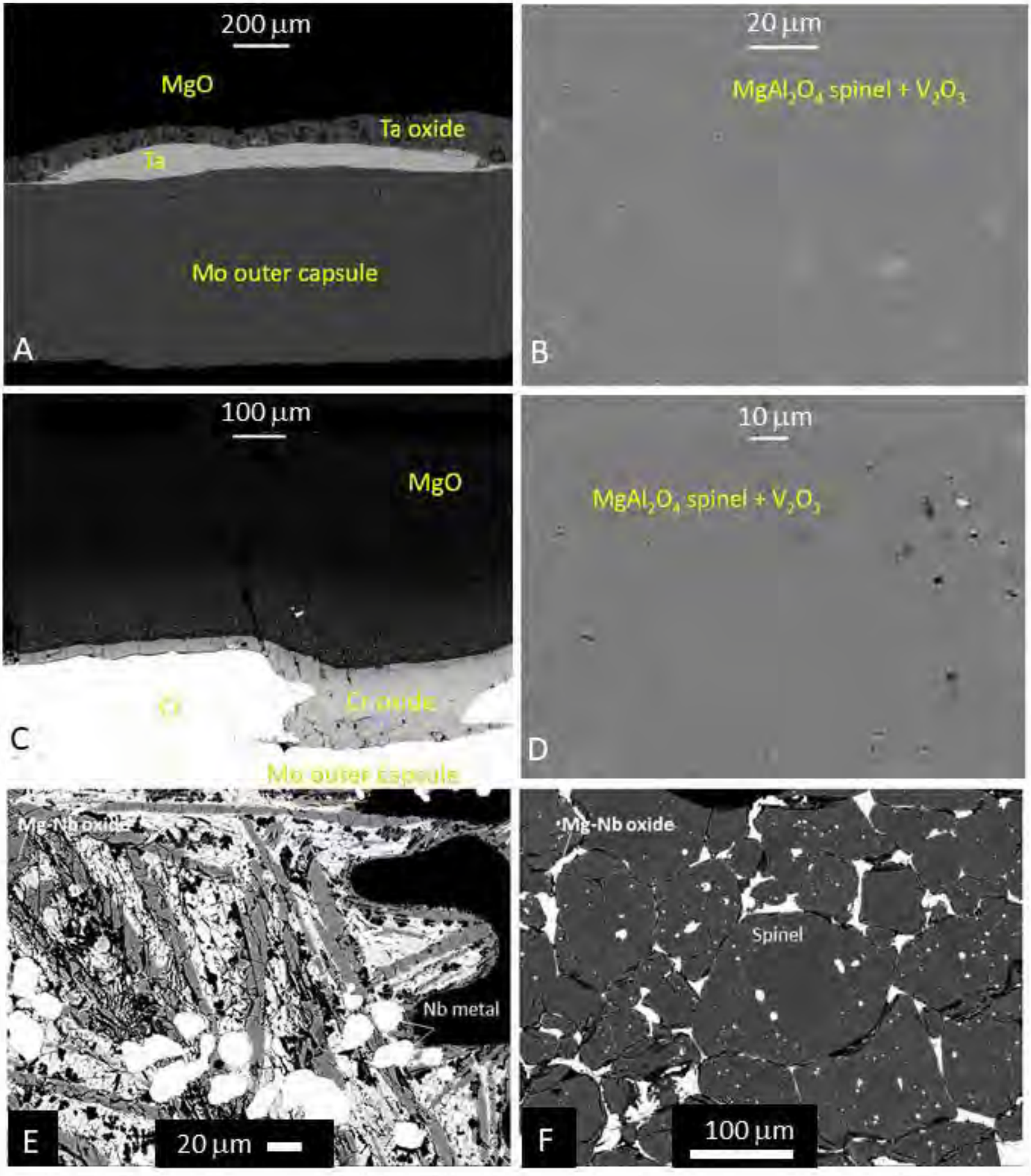
200 µm
MgO
Ta oxide
Ta
Mo outer capsule
A
20 µm
$MgAl_2O_4$ spinel + V_2O_3
B
100 µm
MgO
Cr
Cr oxide
C
Mo outer capsule
10 µm
$MgAl_2O_4$ spinel + V_2O_3
D
Mg-Nb oxide
Nb metal
E
20 µm
Mg-Nb oxide
Spinel
F
100 µm

Figure 7

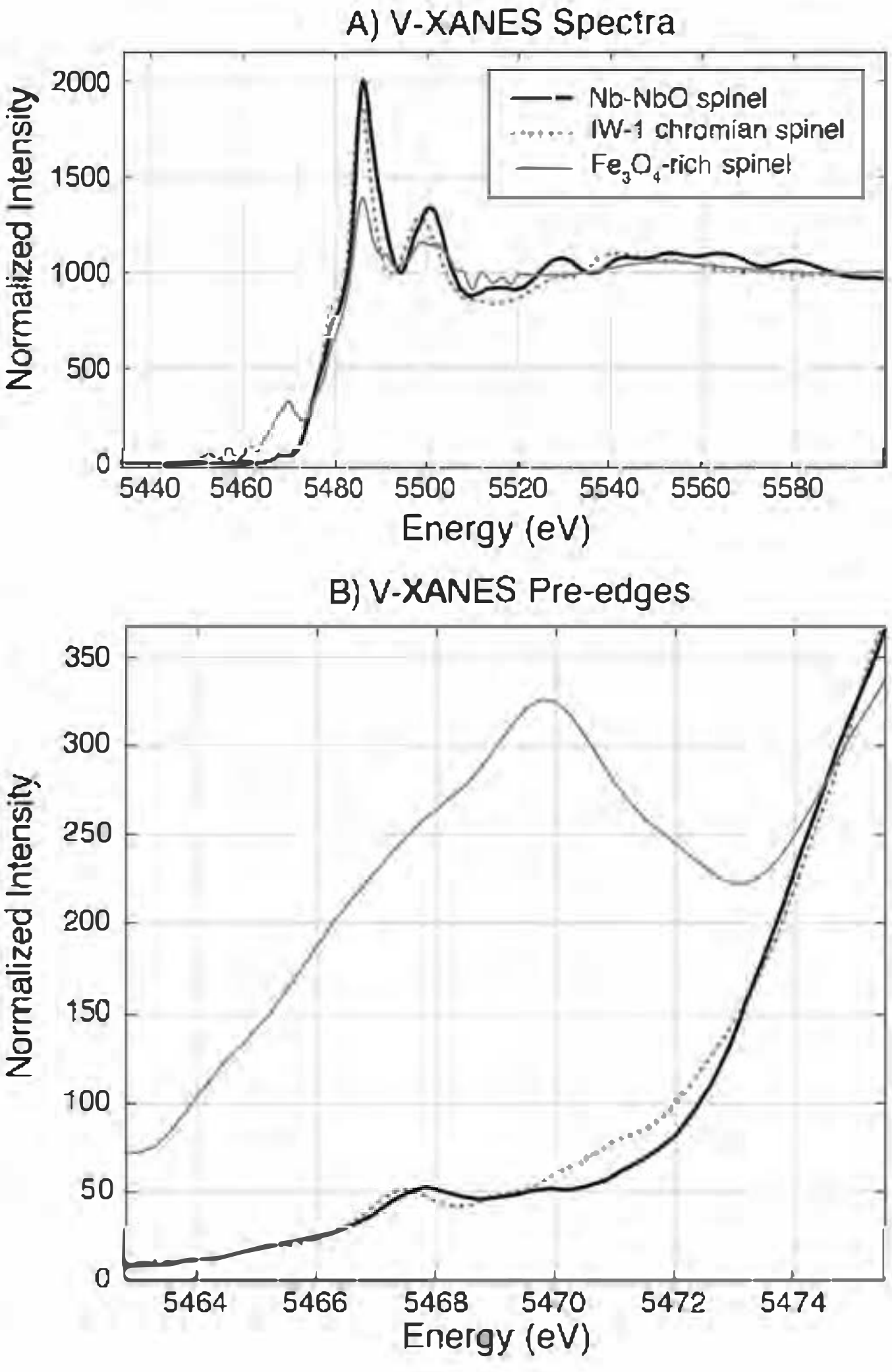
A) V-XANES Spectra
Normalized Intensity
2000
1500
1000
500
0
5440
5460
5480
5500
5520
5540
5560
5580
Energy (eV)
Nb-NbO spinel
IW-1 chromian spinel
Fe3O4-rich spinel
B) V-XANES Pre-edges
Normalized Intensity
350
300
250
200
150
100
50
0
5464
5466
5468
5470
5472
5474
Energy (eV)

Figure 8

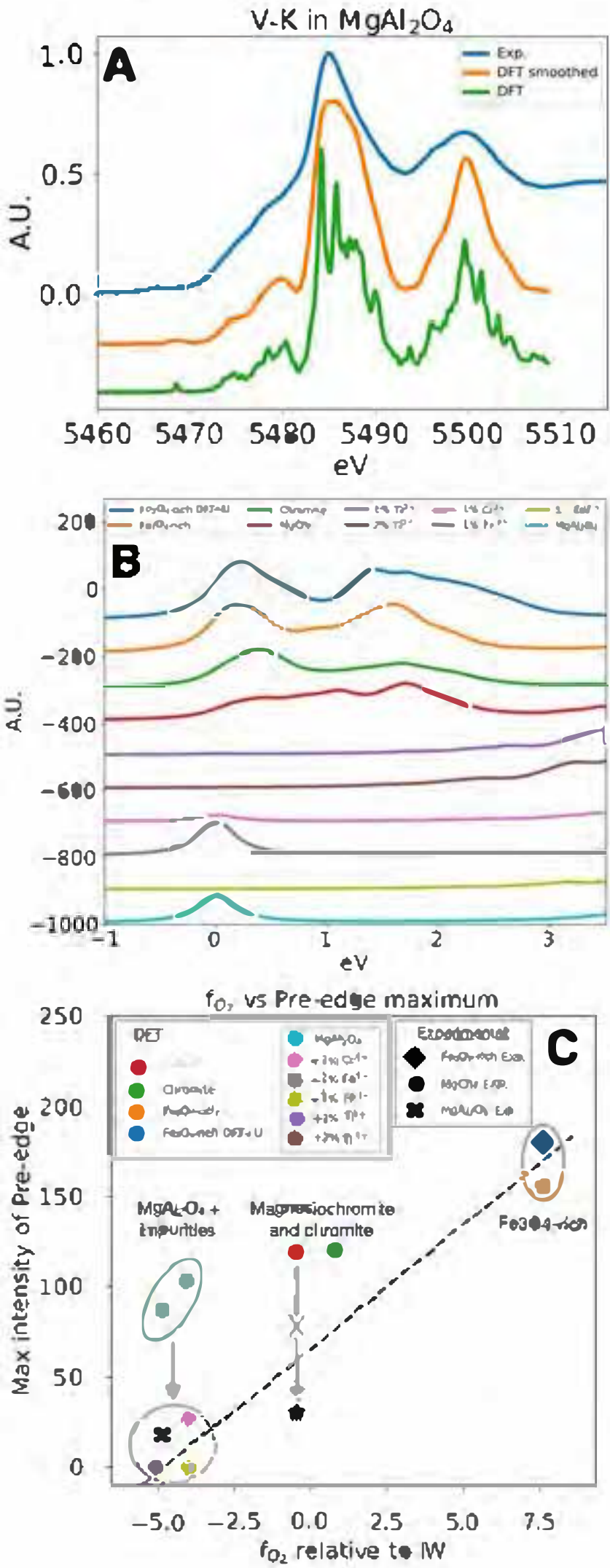
V-K in MgAl2O4
A
Exp.
DFT smoothed
DFT
A.U.
1.0
0.5
0.0
5460 5470 5480 5490 5500 5510
eV
B
A.U.
200
0
−200
−400
−600
−800
−1000
−1 0 1 2 3
eV
f$_{O_2}$ vs Pre-edge maximum
C
DFT
Chromite
Experimental
Max intensity of Pre-edge
250
200
150
100
50
0
MgAl2O4 + impurities
Magnesiochromite and chromite
Fe3O4-rich
−5.0 −2.5 0.0 2.5 5.0 7.5
f$_{O_2}$ relative to IW

Figure 9

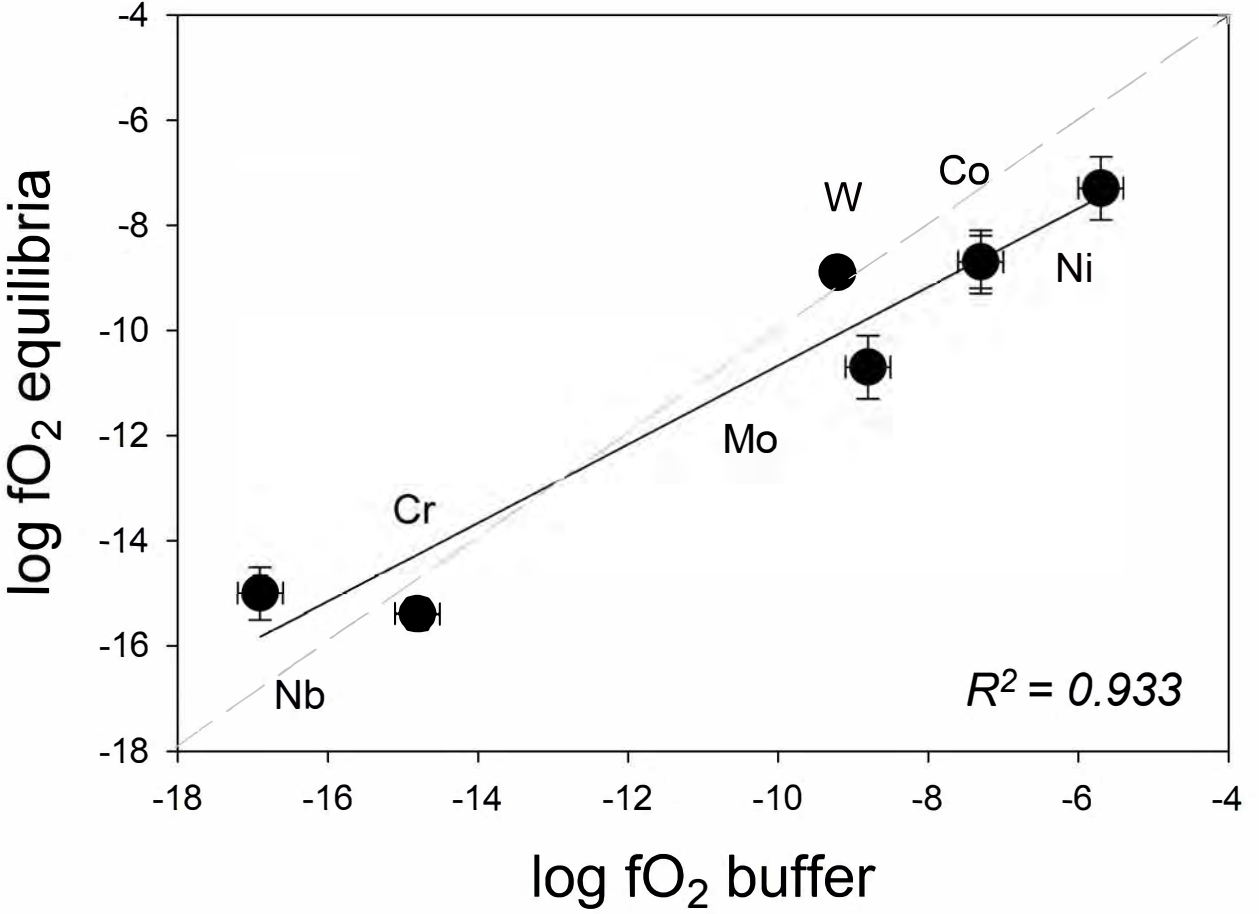
log fO_2 equilibria
log fO_2 buffer
-4
-6
-8
-10
-12
-14
-16
-18
-18
-16
-14
-12
-10
-8
-6
-4
W
Co
Ni
Mo
Cr
Nb
$R^2 = 0.933$

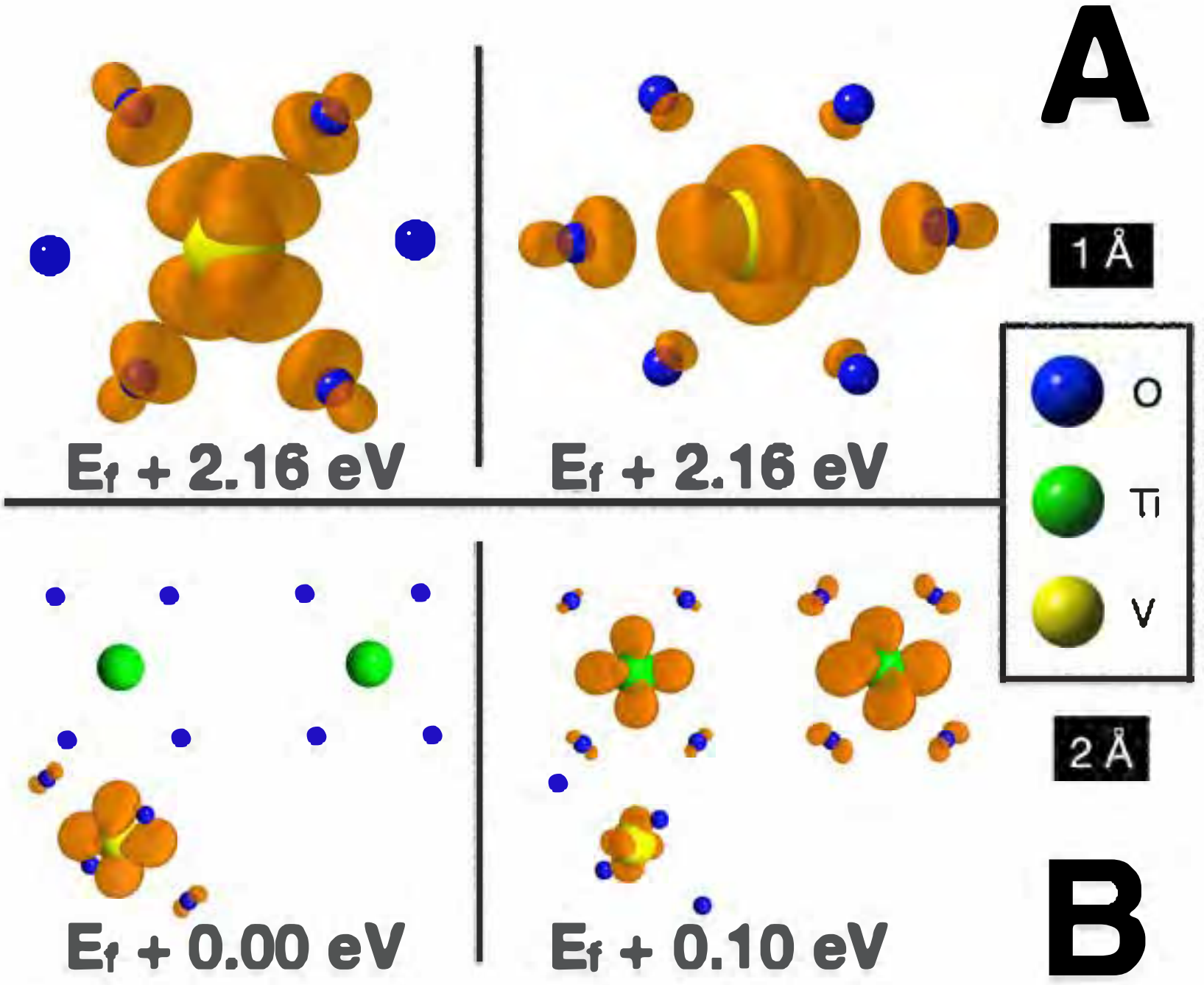

Figure 11

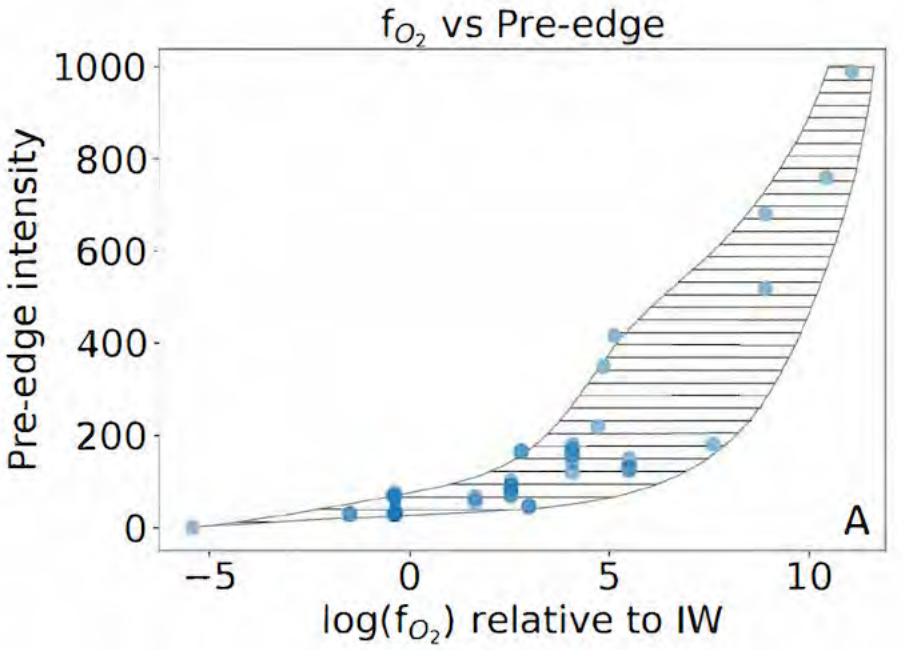
f_{O_2} vs Pre-edge
Pre-edge intensity
1000
800
600
400
200
0
−5
0
5
10
log(f_{O_2}) relative to IW
A

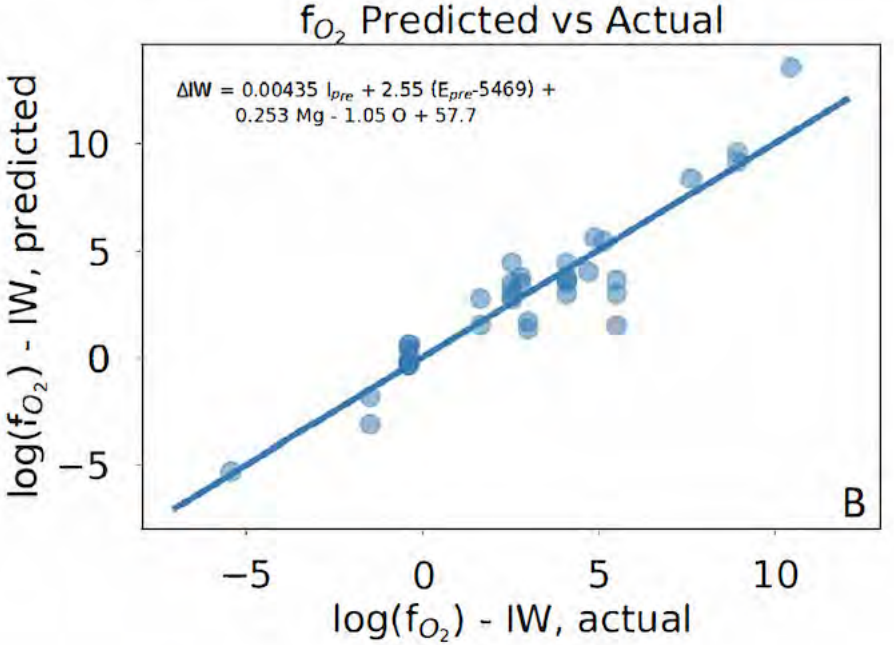
f_{O_2} Predicted vs Actual
ΔIW = 0.00435 I_{pre} + 2.55 (E_{pre}-5469) +
0.253 Mg - 1.05 O + 57.7
log(f_{O_2}) - IW, predicted
10
5
0
−5
−5
0
5
10
log(f_{O_2}) - IW, actual
B

Figure 12